Axisymmetric balance dynamics of tropical cyclone intensification and its breakdown revisited

Roger K. Smith[a,1], Michael T. Montgomery[b] and Hai Bui[c]

[a] *Meteorological Institute, University of Munich, Munich*
[b] *Dept. of Meteorology, Naval Postgraduate School, Monterey, CA* [c] *Department of Meteorology, Vietnam National University, Hanoi, Vietnam*

Abstract:
This paper revisits the evolution of an idealized tropical-cyclone-like vortex forced by a prescribed distribution of diabatic heating in the context of inviscid and frictional axisymmetric balance dynamics. Prognostic solutions are presented for a range of heating distributions, which, in most cases, are allowed to contract as the vortex contracts and intensifies. Interest is focussed on the kinematic structure and evolution of the secondary circulation in physical space and on the development of regions of symmetric and static instability. The solutions are prolonged beyond the onset of unstable regions by regularizing the Sawyer-Eliassen equation in these regions, but for reasons discussed, the model ultimately breaks down. The intensification rate of the vortex is essentially constant up to the time when regions of instability ensue. This result is in contrast to previous suggestions that the rate should increase as the vortex intensifies because the heating becomes progressively more "efficient" when the local inertial stability increases.

The solutions provide a context for re-examining the classical axisymmetric paradigm for tropical cyclone intensification in the light of another widely-invoked intensification paradigm by Emanuel, which postulates that the air in the eyewall flows upwards and outwards along a sloping M-surface after it exits the frictional boundary layer. The conundrum is that the classical mechanism for spin up requires the air above the boundary layer to move inwards while materially conserving M. Insight provided by the balance solutions helps to refine ideas for resolving this conundrum.

1 Introduction

Reduced models have played an important educational role in the fields of dynamic meteorology and geophysical fluid dynamics. These reduced models, traditionally referred to as balance models, are based on rational simplifications of Newton's equation of motion and the thermodynamic energy equation to exploit underlying force balances and thermodynamic balances that prevail in certain large-scale flow regimes (McWilliams 2011, McIntyre 2008) and also in coherent structures, such as atmospheric fronts (Eliassen 1962, Hoskins and Bretherton 1972) and vortical flows (McWilliams et al. 2003).

A scale analysis of the underlying equations for an axisymmetric tropical-cyclone-scale vortex shows that, to a first approximation, the flow is mostly in gradient and hydrostatic balance, and hence in thermal wind balance (Willoughby 1979). Exceptions to this leading order balance include the frictional boundary layer and possibly localized regions in the upper troposphere where the flow may be inertially and/or symmetrically unstable. The validity of the balance approximation has underpinned *the classical theory for tropical cyclone intensification*,

which invokes the convectively-induced inflow through the lower troposphere to draw absolute angular momentum (M) surfaces inwards at levels above the frictional boundary layer, where absolute angular momentum is approximately conserved (Ooyama 1969, 1982: see also Montgomery and Smith 2014, 2017 for up-to-date reviews of paradigms for tropical cyclone intensification). Over the years, the validity of the balance approximation has been exploited in the formulation of numerous idealized theoretical and numerical studies of axisymmetric and weakly asymmetric tropical cyclone behaviour (e.g. Ooyama 1969, Sundqvist 1970a,b, Smith 1981, Shapiro and Willoughby 1982, Schubert and Hack 1982, Hack and Schubert 1986, Schubert and Alworth 1982, Emanuel 1986, Shapiro and Montgomery 1993, Möller and Smith 1994, Montgomery and Shapiro 1995, Möller and Montgomery 2000, Wirth and Dunkerton 2006, Schubert et al. 2007, Rozoff et al. 2008, Pendergrass and Willoughby 2009, Vigh and Schubert 2009, Emanuel 2012, Schubert et al. 2016, Heng and Wang 2016 and many more).

In the case of strictly axisymmetric dynamics, the assumption of thermal wind balance allows the derivation of a single, linear, diagnostic partial differential equation for the streamfunction of the secondary (overturning) circulation in the presence of forcing processes such

[1]Correspondence to: Prof. Roger K. Smith, Meteorological Institute, Ludwig-Maximilians University of Munich, Theresienstr. 37, 80333 Munich. E-mail: roger.smith@lmu.de

as diabatic heating and tangential friction that, by themselves, would drive the vortex away from such a state of balance. This diagnostic equation is often referred to as the Sawyer-Eliassen equation (or SE-equation). Echoing Pendergrass and Willoughby (2009), "a strong, slowly evolving, axially symmetric vortex is a good place to start analysis of tropical cyclone structure and intensity, provided that the analyst recognizes that rapidly changing parts of the flow will generally need to be treated as nonbalanced, perhaps nonlinear, perturbations".

Recent studies of the fluid dynamics of tropical cyclones have shown that the azimuthally-averaged radial flow emerging from the boundary layer in an intensifying tropical cyclone has an outward radial component and, in a broad sense[1], the air in the developing eyewall, itself, is moving upwards and outwards (e.g. Xu and Wang 2010, Fig. 1; Fang and Zhang 2011, Fig. 5; Persing et al. 2013, Figs. 10a,c and 11a,c; Zhang and Marks 2015, Fig. 4; Stern et al. 2015, Figs. 14b and 15b; Schmidt and Smith 2016, Figs. 9b, 10b and 11). In these situations the spin up of the eyewall cannot be explained by the classical axisymmetric mechanism (Schmidt and Smith 2016, Montgomery and Smith 2017). The key question is: could the spin down tendency of radial outflow be reversed by a larger positive tendency from the vertical advection of M *in a balance formulation*[2], or is spin up within a (nonlinear) boundary layer essential to account for the spin up of the eyewall? In either case, the M-surfaces would need to have a negative vertical gradient in the region of net spin up.

Traditionally, the classical model for spin up is presented in terms of axisymmetric balance theory (e.g. Ooyama 1969, Willoughby 1979, Shapiro and Willoughby 1982, Schubert and Hack 1982)[3], which is an example of a reduced model. In order to understand how departures from the balance model might come about in numerical model simulations and in the real world, one needs to know in detail how spin up occurs in the balance model, itself. In particular, one needs to know how the M-surfaces are structured at low levels in the eyewall in this model. Furthermore, one needs to understand the structure of the secondary circulation in relation to these M surfaces.

The foregoing axisymmetric studies of tropical cyclones can be subdivided into ones where a prognostic theory is developed and solved for the vortex evolution (e.g. Ooyama 1969, Sundqvist 1970a,b, Schubert and Alworth 1982, Möller and Smith 1994, Emanuel 1995, 2012, Schubert et al. 2016) and ones where the SE-equation is solved diagnostically for the secondary circulation in the presence of a prescribed forcing mechanism (or mechanisms), possibly with an examination of the instantaneous tangential wind tendency accompanying the calculated overturning circulation (e.g. Smith 1981, Shapiro and Willoughby 1982, Schubert and Hack 1982, Hack and Schubert 1986, Rozoff et al. 2008, Bui et al. 2009, Pendergrass and Willoughby 2009, Wang and Wang 2013, Abarca and Montgomery 2014, Smith et al. 2014). In the former cases, the early studies by Ooyama and Sundqvist incorporated a parameterization of deep cumulus convection, while those of Schubert and Alworth, Möller and Smith used a prescribed heating distribution in the model coordinates: potential radius (R) in the horizontal and potential temperature (θ) in the vertical[4]. The recent study by Schubert et al. (2016) focussed on a highly simplified shallow water model in which the effects of convective heating were modelled as a mass sink as in the one-layer balance model of Smith (1981).

The use of (R, θ)-coordinates leads to an elegant mathematical formulation of the problem, but solutions portrayed in this space can sometimes obscure the underlying physical processes of intensification because the secondary circulation that is fundamental to vortex spin up is implicit in the formulation. The same remark applies to the many theoretical studies by Emanuel (see Emanuel 2012 and refs.), in which the models are formulated also using R-coordinates. For this reason it is useful and insightful to have a prognostic balance formulation in physical coordinates to explore some of the issues referred to above.

In this paper we revisit the dynamics of vortex intensification in the context of a rather general axisymmetric, balanced prediction model. In the formulation, no approximation is made in regard to the variation of density with height or radius and the system is formulated in physical coordinates. The diabatic heating distribution is prescribed, but as in some previous studies, the location of the heating is allowed to move radially-inwards as the vortex contracts. In some simulations the annulus of the heating distribution is vertical and located where it intersects the chosen M-surface that it follows. In other simulations, the axis coincides with the sloping M-surface, itself. In one calculation, the location of the heating is held fixed.

Here the focus is on the kinematic structure and evolution of the primary and secondary circulation in physical space, the amplification of the tangential wind field, and on the ultimate development of localized regions where the flow becomes symmetrically and/or statically unstable. This development heralds the breakdown of the strict balance model because the SE-equation is no longer elliptic

---

[1] Actually, the adjustment of the flow emanating from the boundary layer has the nature of an unsteady centrifugal wave with a vertical scale of several kilometres, akin to the vortex breakdown phenomenon (Rotunno (2014) and refs.) Above the low-level outflow layer there is sometimes an inflow layer that is part of the wave and not directly associated with convectively-driven inflow.

[2] Unless otherwise stated, the term "balance formulation" is used to mean strict gradient wind balance above and within the boundary layer, an assumption that is required by such a formulation, but is a significant limitation of the formulation vis-á-vis reality.

[3] Unlike Ooyama's three-layer formulation on which the classical model is based, Willoughby, Shapiro and Willoughby, Schubert and Hack considered vortices with continuous vertical variation in which the vertical advection of tangential momentum plays a role in spin up also.

[4] The potential radius R is defined by $\frac{1}{2}fR^2 = rv + \frac{1}{2}fr^2$ where r denotes the ordinary radius in a cylindrical polar coordinate system, v the azimuthal (tangential) velocity in this coordinate and f the Coriolis parameter. Note that $R^2 = 2M/f$.

in such regions. Solutions are obtained beyond the time when regions of instability develop by regularizing the SE-equation in these regions to keep it elliptic globally. Ultimately, these extended solutions break down as well for reasons that are explored. Particular interest at all times is centred on the structure of the flow near the base of the eyewall, which, as noted above, provides a context for a more complete understanding of how departures from the classical mechanism come about in numerical models and in observations. The effects of boundary layer friction are examined as well, albeit in the limited context of an axisymmetric balanced boundary layer formulation.

An outline of the remaining paper is as follows. Section 2 reviews briefly the model configuration and method of solution. Section 3 provides a synopsis of the five balance simulations carried out, while Section 4 presents analyses of these simulations. A discussion of the results and the conclusions are given in Section 5.

2 The axisymmetric balance model

As is well known from prior work, the axisymmetric balance model comprises a simplified radial momentum equation expressing strict gradient wind balance, and a simplified vertical momentum equation expressing strict hydrostatic balance. These two balance equations are used in conjunction with an evolution equation for tangential momentum and potential temperature forced, respectively, by sources/sinks of tangential momentum and heat.

Of course, for the balance model to remain physically consistent, the time scales implied by the heat and momentum forcing functions must be long in comparison to the intrinsic oscillation periods of the vortex so as not to excite large-amplitude, high-frequency inertial gravity (centrifugal) modes. Being a balance model, only one of the latter evolution equations can be used to predict the time dependence of the flow. As a result, a compatibility equation must exist to ensure that the tangential velocity and potential temperature remain in thermal wind balance as the vortex evolves under the prescribed forcing. The compatibility equation is the SE-equation for the transverse circulation.

As discussed in Smith et al. (2009) (see footnote on p1718) the balance evolution is easiest to advance forward in time by using the tangential momentum equation. This is because of a restriction on the magnitude of the radial pressure gradient force when solving the gradient wind equation for the tangential velocity.

2.1 The model equations

The specific equations used herein are as follows. The tendency equation for tangential wind component v in cylindrical r-z coordinates is:

$$\frac{\partial v}{\partial t} = -u\frac{\partial v}{\partial r} - w\frac{\partial v}{\partial z} - \frac{uv}{r} - fu - \dot{V}, \quad (1)$$

where u and w are the radial and vertical velocity components, t is the time, f is the Coriolis parameter (assumed constant), and $\dot{V}$ is the azimuthal momentum sink associated with the near-surface frictional stress. Following Smith et al. (2005), the thermal wind equation has the general form

$$\frac{\partial}{\partial r}\log\chi + \frac{C}{g}\frac{\partial}{\partial z}\log\chi = -\frac{\xi}{g}\frac{\partial v}{\partial z}, \quad (2)$$

where $\chi = 1/\theta$ is the inverse of potential temperature θ, $C = v^2/r + fv$ is the sum of centrifugal and Coriolis forces per unit mass, $\xi = f + 2v/r$ is the modified Coriolis (inertia) parameter, i.e. twice the local absolute angular velocity, and g is the acceleration due to gravity. This is a first order partial differential equation for $\log\chi$, which on an isobaric surface is equal to the logarithm of density ρ plus a constant, with characteristics $z_c(r)$ satisfying the ordinary differential equation $dz_c/dr = C/g$.

The SE-equation for the streamfunction ψ has the form:

$$\frac{\partial}{\partial r}\left[-g\frac{\partial\chi}{\partial z}\frac{1}{\rho r}\frac{\partial\psi}{\partial r} - \frac{\partial}{\partial z}(\chi C)\frac{1}{\rho r}\frac{\partial\psi}{\partial z}\right] +$$

$$\frac{\partial}{\partial z}\left[\left(\chi\xi\zeta_a + C\frac{\partial\chi}{\partial r}\right)\frac{1}{\rho r}\frac{\partial\psi}{\partial z} - \frac{\partial}{\partial z}(\chi C)\frac{1}{\rho r}\frac{\partial\psi}{\partial r}\right] =$$

$$g\frac{\partial}{\partial r}\left(\chi^2\dot{\theta}\right) + \frac{\partial}{\partial z}\left(C\chi^2\dot{\theta}\right) + \frac{\partial}{\partial z}\left(\chi\xi\dot{V}\right) \quad (3)$$

where $\zeta = (1/r)\partial(rv)/\partial r$ is the vertical component of relative vorticity, $\zeta_a = \zeta + f$ is the absolute vorticity and $\dot{\theta} = d\theta/dt$ is diabatic heating rate. The derivation of this equation is sketched in section 2.2 of Bui et al. (2009). The transverse velocity components u and w are given in terms of ψ by:

$$u = -\frac{1}{r\rho}\frac{\partial\psi}{\partial z}, \qquad w = \frac{1}{r\rho}\frac{\partial\psi}{\partial r}. \quad (4)$$

As outlined in the appendix, the discriminant of the SE-equation, Δ, is given by

$$\Delta = \gamma^2\left[-\frac{g}{\chi}\frac{\partial\chi}{\partial z}\left(\xi\zeta_a + \frac{C}{\chi}\frac{\partial\chi}{\partial r}\right) - \left(\frac{1}{\chi}\frac{\partial}{\partial z}(C\chi)\right)^2\right], \quad (5)$$

where $\gamma = \chi/(\rho r)$, and the SE-equation is elliptic if $\Delta > 0$.

In the simulations to be described, the prescribed diabatic heating rate has the spatial form:

$$\dot{\theta}(r,z) = \dot{\Theta}\cos\left(\frac{1}{2}\pi\frac{\delta r}{r_i}\right)\cos\left(\frac{1}{2}\pi\frac{\delta z}{Z_M}\right) \quad (r < r_M)$$

$$= \dot{\Theta}\cos\left(\frac{1}{2}\pi\frac{\delta r}{r_o}\right)\cos\left(\frac{1}{2}\pi\frac{\delta z}{Z_M}\right) \quad (r > r_M). \quad (6)$$

where $\delta r = r - r_M$, r_M is the physical radius of the prescribed M surface, r_i and r_o are the inner and outer widths of the heating function, $\delta z = z - Z_M$, Z_M is the height of

maximum heating rate and $\dot{\Theta}$ is maximum amplitude of the heating rate. In all calculations we take $r_i = 20$ km, $r_o = 70$ km, $Z_M = 8$ km and $\dot{\Theta} = 3$ K h^{-1}. Initially, $r_M = 80$ km, but in most cases, this radius varies with time. The different choices for r_i and r_o make the heating rate distribution broader outside the axis of maximum heating than inside. Some of the foregoing values were guided in part by the values diagnosed from a numerical model study of tropical cyclogenesis (Montgomery et al. 2006, Fig. 5(d)). In essence, the heating rate distribution varies sinusoidally with height with a maximum amplitude at an altitude of 8 km and is zero above the tropopause (16 km). In the radial direction, the distribution has a skewed bell-shape in radius (inner radius 20 km, outer radius 70 km scale) and the maximum amplitude of 3 K h^{-1} is centred on a particular M surface.

The effects of surface friction are represented by a body force corresponding with the surface frictional stress distributed through a boundary layer with uniform depth H. The body force has the spatial form:

$$\dot{V}(r,z) = C_d |\mathbf{v}(r,0,t)| v(r,0,t) \exp(-(z/z_0)^2)/H, \quad (7)$$

where C_d is a surface drag coefficient, $\mathbf{v}(r,0,t) = \sqrt{u(r,0,t)^2 + v(r,0,t)^2}$ is the total surface wind speed at time t, and z_0 is a vertical length scale over which the frictional stress is distributed. Here we choose $z_o = 600$ m and $H = 800$ m. This simple formulation is in the spirit of that assumed by Shapiro and Willoughby (1982), but is different from that for a classical boundary layer in that it is strictly balanced and does not have a horizontal pressure gradient that is uniform through the depth of the layer. However, it produces a low level inflow that is qualitatively similar, albeit quantitatively weaker than a more complete boundary layer formulation (Smith and Montgomery 2008).

The vertical thermodynamic structure at large radii is a linear approximation to the Dunion moist tropical sounding (Dunion 2011) as shown in Fig. 1.

For any tangential wind distribution $v(r,z,t)$ and ambient distribution of pressure and temperature as a function of height, a complete balanced solution for a tropical cyclone vortex can be obtained using the unapproximated method of Smith (2006). With the diabatic heating source defined by (6) and frictional drag defined by (7), a solution for the streamfunction of the overturning circulation ψ can be obtained by solving the SE equation (3). Then, u and w can be obtained using Eq. (4). Finally, equation (1) can be integrated to obtain v at the next time step. After each time step, the balanced potential temperature and density fields can be calculated using Eq. (2) by the method of Smith (2006).

2.2 Numerical method

The calculations are carried out in a rectangular domain 1000 km in the radial direction and 18 km in the vertical.

The grid spacing is uniform in both directions, 5 km in the radial direction and 200 m in the vertical. The SE equation is solved using the same successive over-relaxation method as in Bui et al. (2009). The equations are discretized using centered differences, except at boundaries, where forward or backward differences are used as appropriate. A simple Euler scheme is used to time step Eq. (1). The boundary condition on the SE-equation are that $\psi = 0$ at $r = 0$, $z = 0$ and $z = H$, implying no flow through these boundaries, while the outer radial boundary, $r = r_R$, is taken to be open, i.e. $\partial\psi/\partial r = 0$, implying that $w = 0$ at this boundary.

2.3 Regularization of the SE equation

At early times, the discriminant of the SE-equation, Δ, is everywhere positive and the SE-equation is elliptic. However, as time proceeds, isolated regions develop in which Δ becomes negative. In these regions, the SE-equation is hyperbolic and the flow there satisfies the conditions for symmetric instability. Technically, the SE-equation has reached an impasse and loses solvability as a balance problem. To advance the solution beyond this time a regularization method is required. The regularization scheme used here is similar to that proposed by Möller and Shapiro (2002) and used by Bui et al. (2009). It is discussed in the Appendix.

The fact that one can still obtain a solution with an *ad-hoc*, minimal regularization method allows one to extend the balance solution beyond this loss of solvability. However, it is not strictly correct to speak of these solutions as "balanced solutions" in the ordinary elliptic sense since they are instead more like "weak" solutions and their structure/magnitude near the symmetric instability or statically unstable regions will depend on how the regularization is formulated.

3 Five simulations

Table I. Summary of the five simulations

Simulation	Heating distribution	Friction
Ex-U	Upright	no
Ex-US	Upright, stationary	no
Ex-S	Slantwise	no
Ex-FO	No heating	yes
Ex-UF	Upright	yes

We present the results of five simulations, which are summarized in Table I. Each simulation starts with an initial warm-cored vortex that has a maximum tangential wind speed of 10 m s^{-1} at the surface at a radius of 100 km at a latitude of 20°N. The time step for the calculation is 1 minute.

In three simulations, Ex-U, Ex-US and Ex-UF the diabatic heating rate has a vertical axis intersecting a chosen M-surface at a height of 1 km and moves inwards
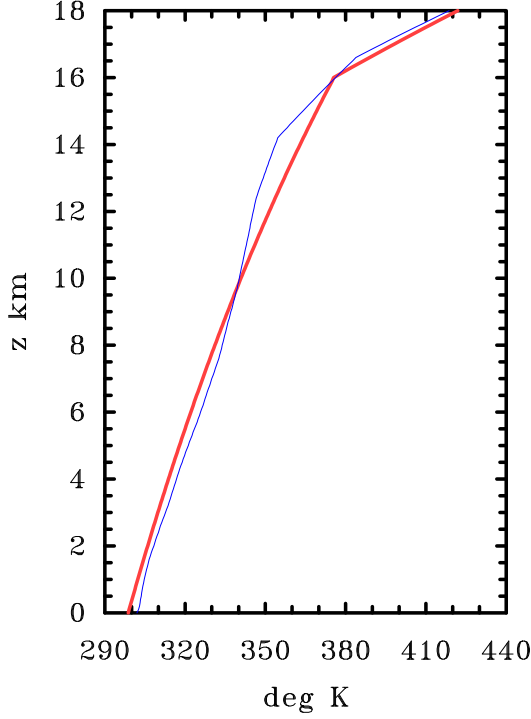
Figure 1. Far field sounding of $\theta(z)$ (thick red curve) compared with that for the Dunion tropical sounding (thin blue curve).

Figure 2. Time series of (a) V_{max}, (b) U_{max} (red) , U_{min} (blue) for Ex-U (solid curves) and Ex-US (dashed curves). The vertical line indicates the time at which the regularization is first required, which is essentially the same for the two experiments (1 min. difference).

with this M-surface as the vortex evolves. This M-surface, which corresponds with a potential radius of 265 km, is located initially inside the radius of maximum tangential wind speed. The configuration of the simulations Ex-US and Ex-UF are the same as Ex-U, except that in Ex-US, the location of the heating distribution is held fixed in space, while in Ex-UF, a representation of near-surface friction is included ($\dot{V} \neq 0$). In Ex-S, the axis of the diabatic heating rate is aligned along the chosen M-surface and slopes upwards and outwards with height, but friction is excluded ($\dot{V} = 0$). The slope of the heating is arguably more realistic for the mature stage of tropical cyclone development. In Ex-FO, there is no heating and only friction.

4 Results

4.1 Vortex evolution in the Ex-U calculation

Figure 2 shows time series of the maximum tangential velocity component, V_{max}, the maximum radial velocity component, U_{max}, and the magnitude of the (negative) minimum radial velocity component U_{min} for the calculations Ex-U and Ex-US. We focus first on Ex-U and discuss Ex-US in section 4.2. In Ex-U, V_{max} increases essentially linearly with time at a rate of approximately 13 m s^{-1} (24 h)$^{-1}$ up to about 9 h. Thereafter, the rate increases, slowly until about 17 h and more rapidly at later times. The integration terminates a little after 24 h for reasons that are discussed later. At 24 h, V_{max} has attained a value of about 29 m s^{-1}. At $t = 0$ h, both U_{max} and $U_{min}(t)$ have a value of
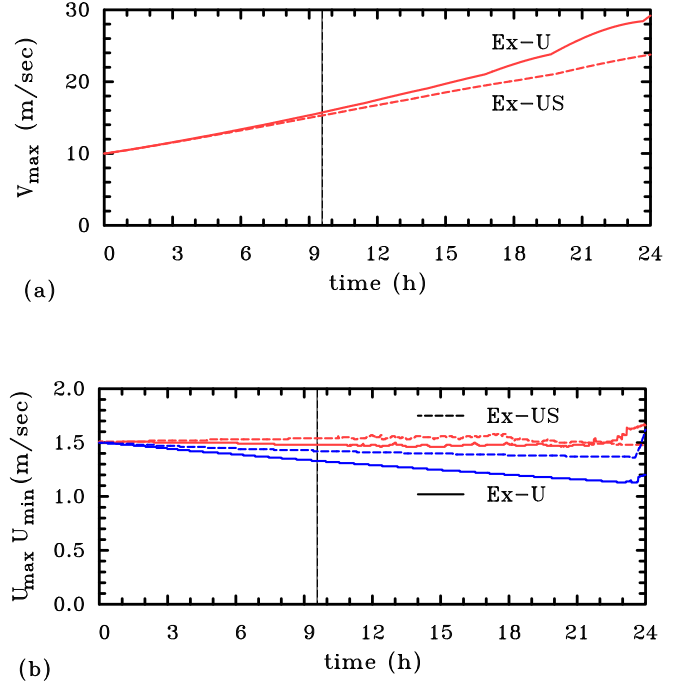
1.5 m s^{-1}. Thereafter, $U_{min}(t)$ declines slowly and approximately linearly until shortly before 24 h, when it increases slightly, and U_{max} remains approximately constant until 22 h, when it begins to increase also.

The vertical lines in Figs. 2a and 2b indicates the first time at which the discriminant in the SE-equation, Δ, becomes negative at some point in the domain for the particular experiment. Beyond this time, the regularization procedure detailed in the Appendix is applied to remove the initially small regions where the flow would be symmetrically unstable.

4.1.1 Stream flow and velocity fields

Figures 3-6 show radius-height cross sections of the M-surfaces superimposed on various fields at the initial time and at 9 h, before the regularization procedure is first required. Panels (a) and (b) show the distribution of heating rate $\dot{\theta}$ as well as the streamfunction of the secondary circulation, ψ. As noted above, the $\dot{\theta}$ distribution is tied to a prescribed M surface at a height of 1 km. This M-surface moves inwards from about 80 km at $t = 0$ h to 69 km at $t = 9$ h. Outside the heating region, the flow is quasi-horizontal with inflow in the lower troposphere, below about 5 km, and outflow above this level. In the lower troposphere, the M-surfaces are advected inwards in accord with the classical mechanism of intensification. Most of the inflow passes through the region of heating and at low to mid-levels the flow has a significant component across the M-surfaces in the direction towards decreasing M. Thus the vertical
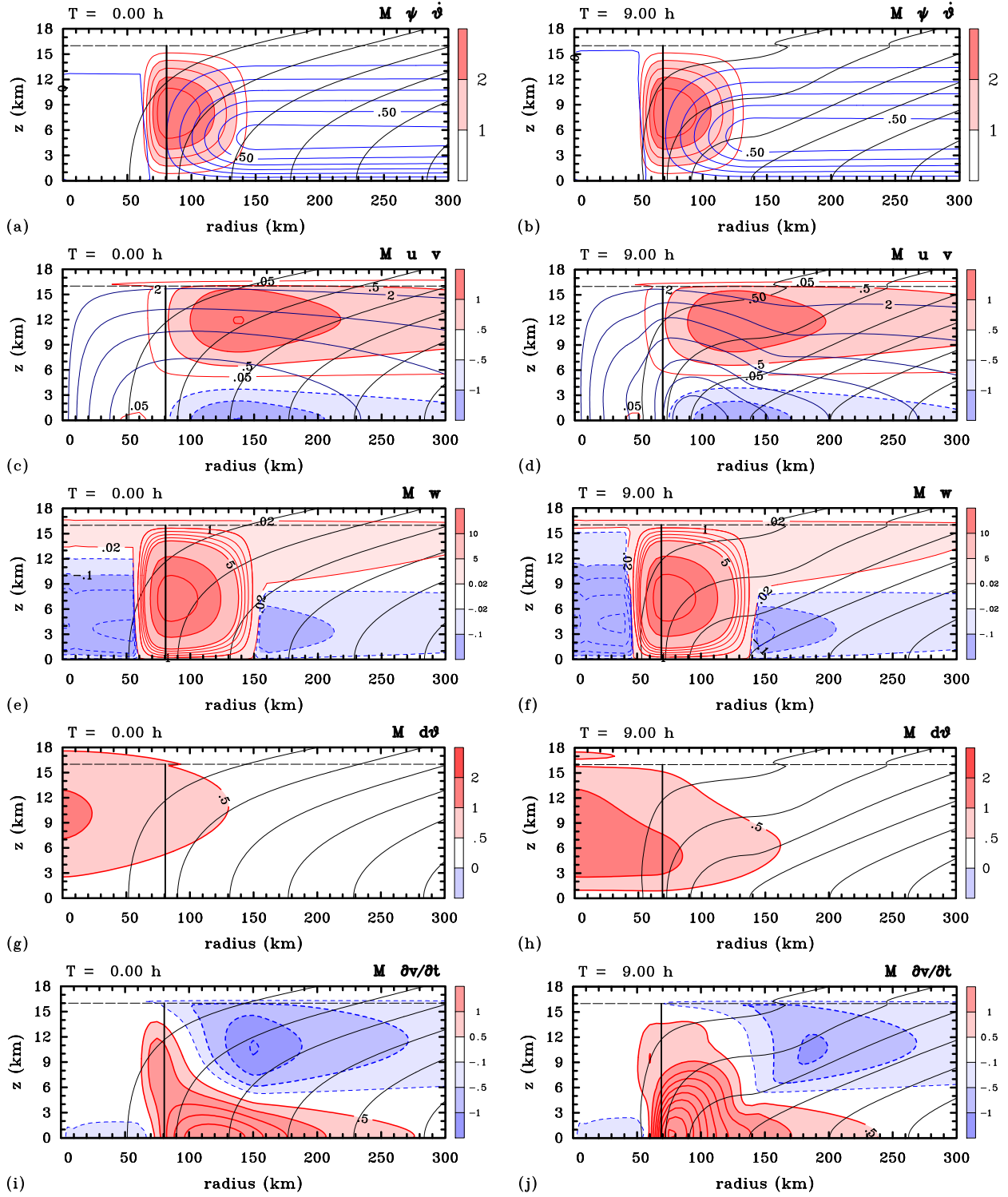
Figure 3. Radial-height cross sections of M-surfaces superimposed on various quantities for the simulation Ex-U. These quantities include: (a,b) streamlines of the secondary circulation, ψ, and diabatic heating rate $\dot{\theta}$ (shaded); (c,d) contours of tangential velocity, v, and radial velocity u (shaded); (e,f) contours of vertical velocity, w (shaded); (g,h) contours of potential temperature perturbation, $\theta' = \theta(r, z) - \theta(R, z)$ (shaded), and (i,j) the tangential wind tendency, $\partial v/\partial t$ (shaded). The left panels are at the initial time and the right panels are at 9 h. The dashed horizontal line at a height of 16 km indicates the tropopause. The thick vertical line shows the location of the maximum diabatic heating rate. Contour intervals are: for M, 5×10^5 m^2 s^{-1}; for ψ, 1×10^8 kg s^{-1}; for $\dot{\theta}$, 0.5 K h^{-1}; for u, 0.5 m s^{-1}, 0.02 m s^{-1} (thin solid contours below 2.5 km height and inside 75 km radius), 1 m s^{-1} for negative values dashed contours; for v, 2 m s^{-1}; for w, positive values: 5 cm s^{-1} (thick contours), 1 cm s^{-1} to 4 cm s^{-1} (thin contours) and 0.2 mm s^{-1} (very thin contour), negative values 2 mm s^{-1} (thin contours), 1 mm s^{-1} and 0.2 mm s^{-1} (very thin contours); for θ', 0.5 K; and for $\partial v/\partial t$, 0.5 m s^{-1} (6 h)$^{-1}$ (thick contours), 0.1 m s^{-1} (6 h)$^{-1}$ (thin contour). For all fields: positive values (solid), negative values (dashed).

advection of M becomes important in spinning up the flow there. This behaviour is consistent with the statement of Pendergrass and Willoughby (2009) (p. 814) that the acceleration of the tangential wind "is primarily caused by upward and inward advection of angular momentum"[5]. This finding is consistent also with that in a recent study by Paull et al. (2017).

Panels (c) and (d) of Fig. 3 show the radial and tangential velocity components in relation to the M-surfaces. The maximum tangential wind speed occurs at the surface where the inflow is a maximum. This is to be expected because V_{max} lies at the surface initially and U_{min} occurs at the surface at subsequent times. Thus, the largest inward advection of the M-surfaces occurs at the surface. The asymmetry in the depths of inflow and outflow is a consequence of mass continuity and the fact that density decreases approximately exponentially with height. The maximum outflow occurs at a height of about 12 km.

Figures 3e and 3f show the vertical velocity w in relation to the M-surfaces. At both times shown, there is strong ascent in the heating region and weak ascent in the upper troposphere at all radii, except below 13.5 km inside the heating region. In the lower and middle troposphere, there is subsidence both inside and outside the heating region. The maximum vertical velocity is about 18 cm s^{-1} and it occurs at a height of about 7 km. The subsidence is strongest at low levels inside the heating region, the maximum being 4.3 mm s^{-1} at $t = 0$. As time proceeds, the subsidence both inside and outside the heating region increases in strength as the radius of the heating region contracts. The maximum subsidence at $t = 9$ h is 6.4 mm s^{-1} and occurs just outside the heating region.

4.1.2   Potential temperature perturbation

Figures 3g and 3h show the perturbation potential temperature, $\theta' = \theta(r, z) - \theta(R, z)$, relative to the ambient potential temperature profile at the outer boundary, $(r = R)$. At $t = 0$, the warm anomaly in balance with the tangential wind field has a maximum of 1.1 K located on the rotation axis at an altitude of 10 km. By 9 h, the warm anomaly has strengthened throughout the vortex core and the maximum, now 1.4 K, has shifted downwards to 6.2 km, again on the vortex axis.

4.1.3   Tangential wind tendency

Figures 3i and 3j show the local tangential wind tendency $\partial v / \partial t$, obtained by evaluating the terms on the right hand side of Eq. (1), which, after rearrangement, represent $1/r$ times the advection of the M-surfaces by the secondary circulation, at least in the present calculation when $\dot{V} = 0$. At both $t = 0$ h and $t = 9$ h there is a strong positive tendency in the lower troposphere within and outside the region of

heating and a tongue extending to the high troposphere about the axis of heating. This positive tendency, which coincides with the region where the flow in Fig. 3a and 3b is across the M surfaces in the direction of decreasing M, is a maximum at the surface, but extends through an appreciable depth of the heating region (over 13 km in altitude at 9 h). The tendency is negative in the upper troposphere, typically above an altitude of 6 km and mostly beyond the heating region, where the flow crosses the M surfaces in the direction of increasing M. This negative tendency is strongest at levels where the outflow is strong (compare panels (i) and (j) of Fig. 3 with panels (c) and (d), respectively). At low levels inside the axis of maximum heating there is a small spin down tendency due to the weak outflow under the main updraught (see panels (c) and (d)). A similar pattern of outflow at low levels in the eye region was found by Pendergrass and Willoughby (2009), see their Fig. 5.

One notable feature at both times is the overlap between positive tendency and radial outflow, principally within the upper troposphere in the region of heating (compare again panels (i) and (j) of Fig. 3 with panels (c) and (d), respectively), but the largest positive tendencies occur in the lower troposphere where the radial flow is inwards.

4.1.4   Potential temperature and discriminant

Figures 4a and 4b show isentropes of potential temperature, θ, in relation to the M-surfaces at $t = 0$ h and $t = 9$ h. They show also the values of Δ at these times. Notably, the θ surfaces are close to horizontal at both times, even though they dip down slightly in the inner region reflecting the warm core structure of the vortex. At neither times are there regions of static instability. At $t = 0$ h, Δ decreases monotonically as a function of radius and, like θ, has a sharp positive vertical gradient at the tropopause. At $t = 9$ h, there is closed region of low values of Δ in the middle troposphere at a radius of about 140 km.

4.1.5   Potential vorticity

To gain insight into the factors responsible for the evolution of Δ, and in particular its eventual change from positive to negative values just outside the maximum heating axis, it proves useful to recall the dynamics of dry Ertel potential vorticity (PV). For an axisymmetric flow expressed in cylindrical-polar coordinates, the PV is given by the formula

$$PV = \frac{1}{\rho} \left(-\frac{\partial v}{\partial z} \frac{\partial \theta}{\partial r} + \zeta_a \frac{\partial \theta}{\partial z} \right). \qquad (8)$$

where ζ_a denotes the absolute vertical vorticity. The relation between Δ and PV was shown in Bui et al. (2009) to be:

$$\xi PV = \frac{1}{\rho g \chi^3} \Delta. \qquad (9)$$

From this equation it is evident that the evolution of Δ is intimately tied to those of PV and the inertia parameter, ξ. For all examples considered here, the tangential velocity

---

[5]These authors made this inference from the fields of balanced tangential wind tendency, but did not show the structure of the M-surfaces in relationship to the streamlines.
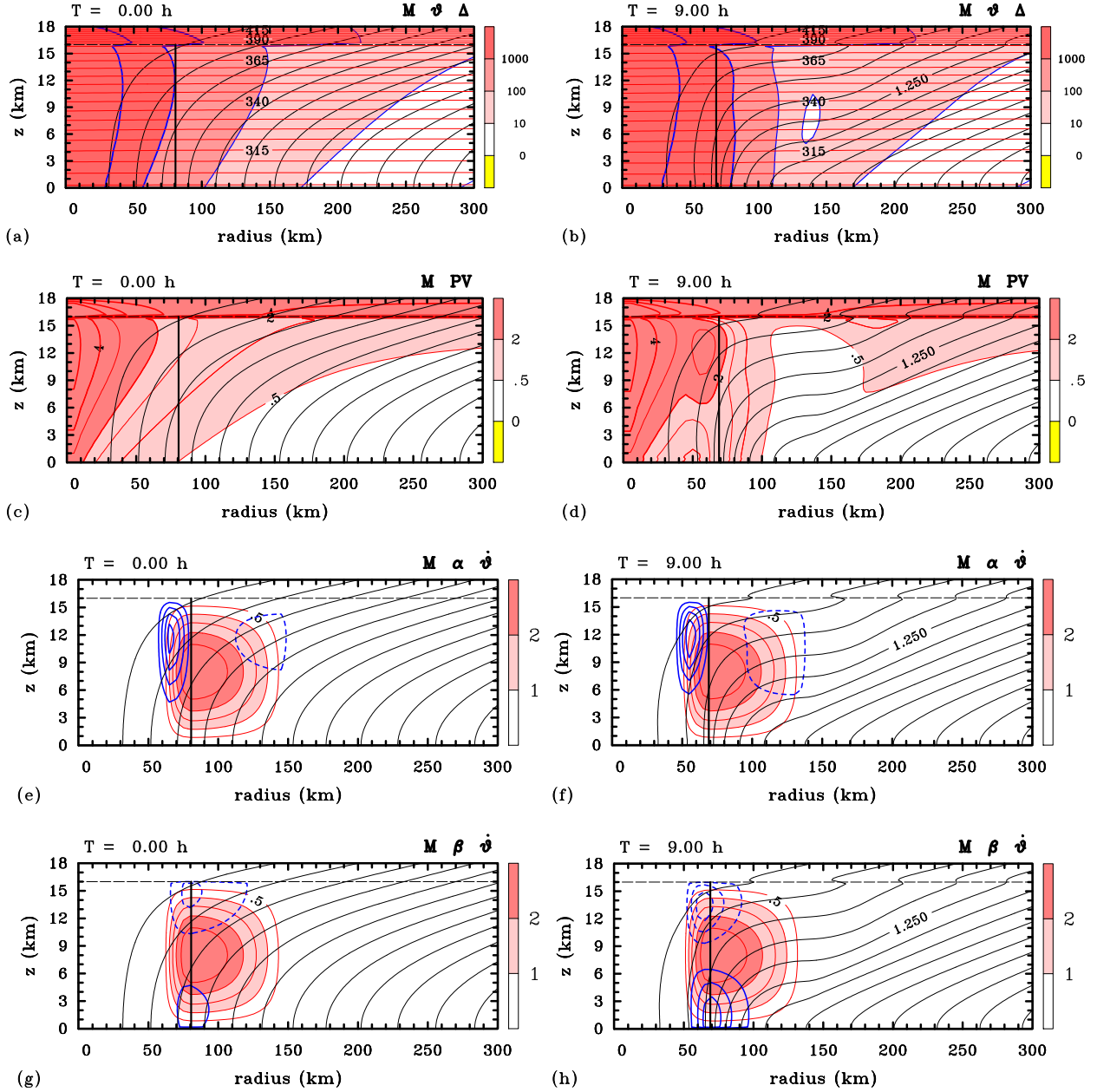
Figure 4. Radius-height cross sections of M-surfaces superimposed on additional quantities for the simulation Ex-U. These quantities include: (a,b) isentropes and the discriminant of the SE-equation D (shaded); (c,d) potential vorticity, PV (shaded); (e,f) the forcing term α in the PV-tendency equation (Eq. 10) superimposed on $\dot{\theta}$ (shaded); and (g,h) the forcing term β in the PV-tendency equation superimposed on $\dot{\theta}$ (shaded). Contour intervals are: for M 5×10^5 m^2 s^{-1}; for δ, 1×10^{-28} unit (very thin contour), 1×10^{-27} and 1×10^{-26} units (thin contour), 1×10^{-25} and 1×10^{-24} units (thick contours), where 1 unit has dimensions m^4 s^{-2} kg^{-2} K^{-2}; for PV, 1 PV unit (= 1×10^{-6} m^2 s^{-1} K kg^{-1}); for θ, 5 K; for $\dot{\theta}$, 0.5 K h^{-1}; for α and β, 1×10^{-10} m^2 s^{-1} K kg^{-1}.

is cyclonic except in the outflow anticyclone. Nevertheless, $\xi > 0$ everywhere, even where $v < 0$, so that the only way for Δ to become negative is for the PV to become negative.

Figures 4c and 4d show radius-height cross sections of the PV distribution at $t = 0$ h and $t = 9$ h. At $t = 0$ h, the PV is a monotonically decreasing function of radius in the troposphere and has large values in the stratosphere on account of the large static stability there. However, at

9 h, an extensive region of low PV values has formed in an annulus extending between about 100 km and 170 km throughout the troposphere. This region is approximately centred on the region of low Δ values seen in Fig. 4b.

To understand how anomalously low (and eventually negative) PV can arise from an initially everywhere positive PV, we recall the equation for the material rate of
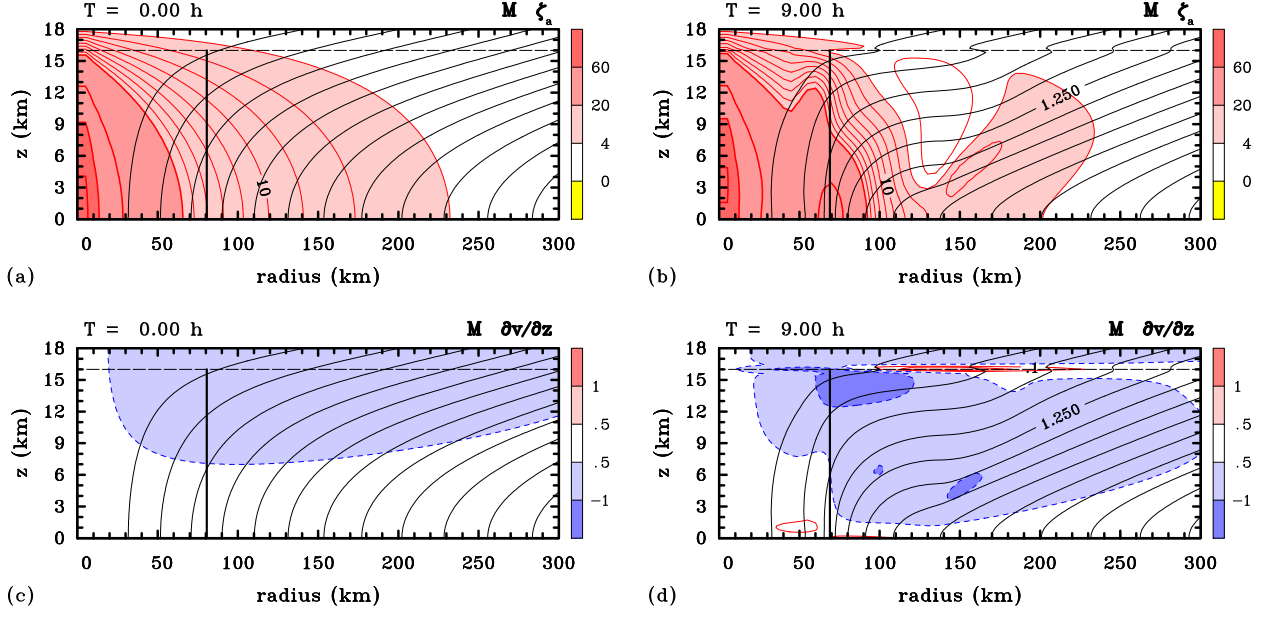
Figure 5. Radius-height cross sections of M-surfaces superimposed on various quantities for the simulation Ex-U. These quantities include: (a,b) contours of absolute vorticity ζ_a (shaded); (c,d) contours of the vertical shear $\partial v/\partial z$. The left panels are at the initial time and the right panels are at 9 h. Contour intervals are: for M, 5×10^5 m^2 s^{-1}; for ζ_a 10^{-5} s^{-1}; for $\partial v/\partial z$ 5×10^{-5} s^{-1} (thin red contours 1×10^{-5} s^{-1} and 5×10^{-5} s^{-1}).

change of PV for an axi-symmetric flow:

$$\frac{D}{Dt}PV = \frac{1}{\rho}\left(-\frac{\partial v}{\partial z}\frac{\partial \dot{\theta}}{\partial r} + \zeta_a\frac{\partial \dot{\theta}}{\partial z}\right). \qquad (10)$$

where $D/Dt = \partial/\partial t + u\partial/\partial r + w\partial/\partial z$ is the material derivative operator. Figures 4e-h show the two contributions on the right hand side of Eq. (10) to the material rate of change of PV at $t = 0$ and $t = 9$ h. The first term $\alpha = (-1/\rho)(\partial v/\partial z)(\partial \dot{\theta}/\partial r)$ represents the local generation/destruction of PV by the radial vorticity component times the radial gradient of diabatic heating, because, for an axisymmetric flow, $\partial v/\partial z$ is equal to minus the radial component of relative vorticity. The second term $\beta = (\zeta_a/\rho)(\partial \dot{\theta}/\partial z)$ represents the concentration/dilution of pre-existing PV by the vertical gradient of diabatic heating. At both times shown, the structure of α exhibits a radial dipole-like structure with a positive PV tendency just inside the axis of maximum heating in the mid to upper troposphere, and a somewhat weaker negative PV tendency beyond the heating axis at roughly similar altitudes. The structure of β shows a positive PV tendency at low-levels and a negative PV tendency at upper-levels centred along the axis of maximum heating. This structure resembles a vertical dipole and reflects the positive vertical gradient of heating at low levels and the negative vertical gradient at upper levels above the heating axis. The combined effect of the β and α terms is to produce an annulus of elevated (cyclonic) PV in the lower part of the heating region and reduced values of PV on the outer side of this annulus.

4.1.6 Vertical vorticity

Given the evolution of Δ and PV shown above, the evolution of vertical vorticity is of some interest also. Figures 5a and 5b show cross sections of absolute vorticity, ζ_a, in relation to the M-surfaces. At $t = 0$, ζ_a is everywhere positive and like the PV has a broad monopole structure (i.e. it decreases monotonically with radius). However, at 9 h, the initially cyclonic ζ_a has become amplified in an annular region centred on the axis of diabatic heating and a region of low values has developed beyond the axis of maximum heating rate, mostly above 3 km. This region is clearly related to that of low values of Δ in Fig. 4b and PV in Fig. 4d.

4.1.7 Vertical wind shear

Figures 5c and 5d show the contours of vertical shear of the tangential wind component, $\partial v/\partial z$. At $t = 0$, the vertical shear is negative and the region of significant shear lies in the upper troposphere (panel (c)), whereas, by 9 h, regions of stronger negative shear have developed, the most prominent being in the upper part of the heating region (panel (d)). At the same time, thin layers of enhanced negative shear inside the heating region and of positive shear beyond the heating region have developed along the tropopause. In addition, a shallow region of positive shear has developed inside the heating region just above the surface. This positive shear is associated with the radially-outward advection of the M-surfaces by the shallow outflow in this region seen in Fig. 3c, while the deeper region of negative shear seen
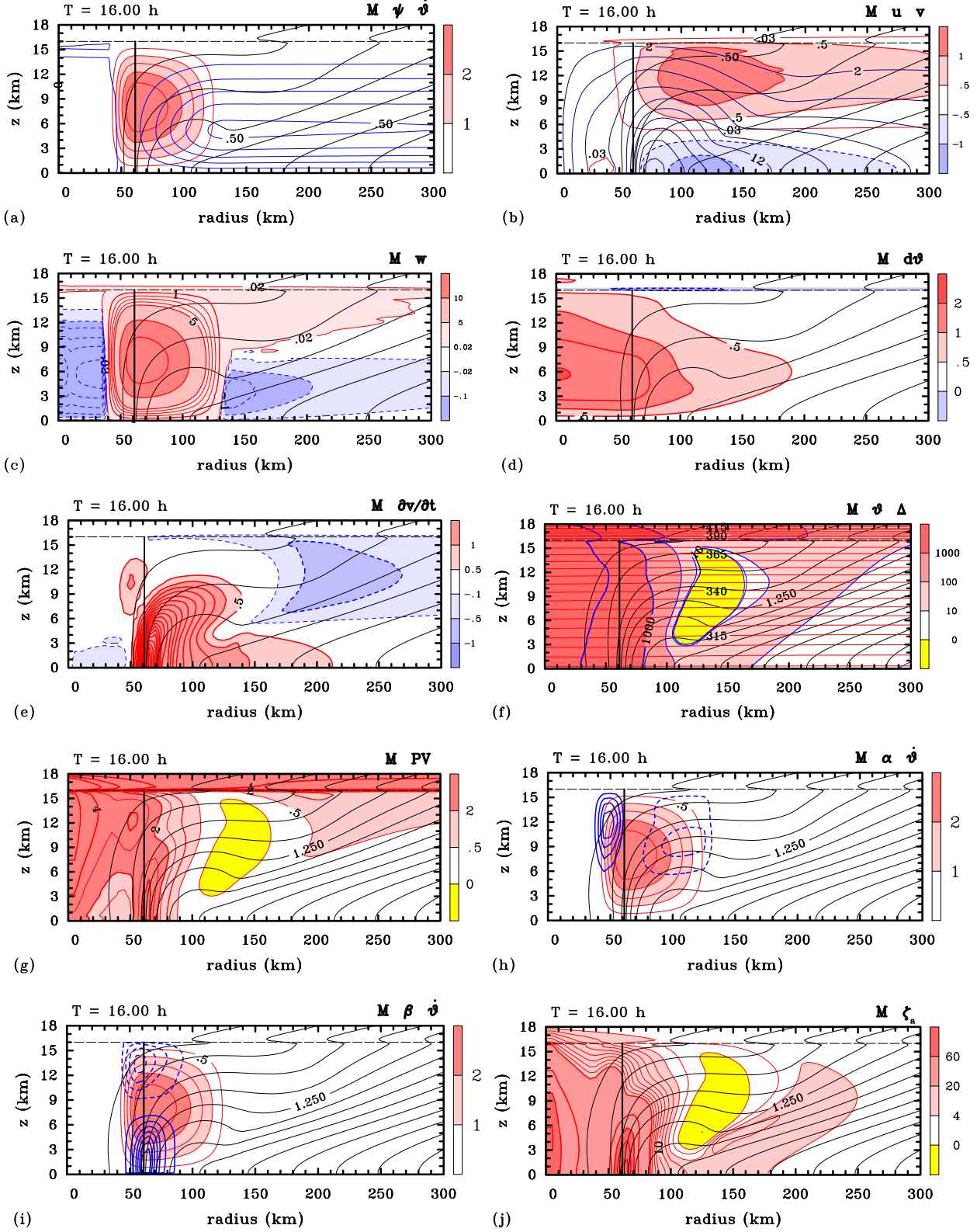
Figure 6. Radial-height cross sections for Ex-U as for panels (a), (c), (e) and (g) in Fig. 3 and panels (a), (c), (e), (g) in Fig. 4 except at 16 h, nearly 7 h after regularization is required. The thin contour in panel (b) is 0.03 m s^{-1}, unlike in panels (c) and (d) of Fig. 3.

in Fig. 5(d) is associated with the differential advection of
the M-surfaces by the heating-induced inflow, which is a

maximum near the surface.

4.1.8 Development of symmetrically-unstable regions

Figure 6 shows radius-height cross sections of selected quantities similar to those in Figs. 3-5, but at 16 h, more than 6 h after a region of symmetric instability has developed and the SE-equation requires regularization. Even at this time, the fields are generally smooth. The axis of heating has moved further inwards to just over 60 km radius and some of the M surfaces have folded in the mid and upper troposphere to form a "well-like" structure beyond the heating region, partly because of differential vertical advection of the M-surfaces between the ascending branch of the secondary circulation and the region of subsidence outside the heating. Some distance inwards from the lowest point of the well, the radial gradient of M is negative, implying negative absolute vorticity and thereby inertial instability. It is interesting that, even at this stage of evolution, the M-surfaces are generally not congruent with the streamlines in the upper troposphere as they would have to be if the flow were close to a steady state.

Notably, the subsidence inside the heating region has strengthened (panel (c)) and the eye has warmed further (panel (d)), θ' now being 2 K at a height of 5.8 km compared with 1.4 K at a height of 6.2 km at 9 h. The tangential wind tendency has increased further and remains positive at the location of V_{max} (compare panels (e) and (b)) consistent with the continued increase in V_{max} seen in Fig. 2. Positive tendencies in the region of heating continue to extend above 11 km and at larger heights, these positive tendencies overlap with regions of outflow, highlighting the importance of the vertical advection on M in spinning up this region.

At 16 h, the regions of low Δ, PV and ζ_a seen in Figs. 4 and 5 have become more pronounced and regions where these quantities are negative have formed (Figs. 6f, 6g and 6j). As noted above, the region of negative ζ_a coincides with that in which the M-surfaces dip down with increasing radius and because the static stability does not reverse sign anywhere (panel(f)), the region of inertial instability is one also of symmetric instability in which both Δ and PV are negative. Panels (h) and (i) of Fig. 6 show similar patterns of PV generation as in panels (e), (f) and (g), (h), respectively, of Fig. 4. Because, in the absence of heating, PV is materially conserved, the occurrence of regions of negative PV must be a result of the negative generation of PV in the upper troposphere, which is another way of viewing the formation of a region of symmetric instability.

4.1.9 Ultimate solution breakdown

The breakdown of the regularized solution shortly after 24 h is brought about by the appearance and growth of small-scale features in the secondary circulation in the upper troposphere, near the edge of where $\Delta < 0$ (not shown). The small-scale features arise from spatial irregularities introduced by the ad-hoc regularization method described in the Appendix. This regularization procedure is necessarily

somewhat arbitrary and only removes conditions for symmetric instability in the SE-equation and not in the equation for the tangential wind tendency. As a result, regions of inertial instability with negative values of ζ_a are still seen by the tendency equation and inertial instability can still manifest itself during the flow evolution. Typically, regions of static instability occur only in the presence of friction and with our method here, they tend to lead to a catastrophic breakdown of the solution very rapidly.

Eventually, a time is reached when M becomes negative at some point, presumably on account of numerical issues. At this point, the solution is programmed to terminate. While it may be possible to extend the solution beyond this point for some time interval by refining the numerical algorithm (and in part smoothing the coefficients in the SE-equation after each regularization step), the main purpose of our study is to understand how the axisymmetric balance solution, itself, breaks down and not to devise necessarily *ad hoc* ways to extend the solution.

If, for the sake of argument, such a continuation method could be developed, we would expect to see continued sharpening of the radial gradient of M at the base of the updraught as air is drawn into the updraught from both sides near the surface. In essence, the flow there is trying to form a discontinuity in M (and a corresponding vortex sheet) by a process akin to frontogenesis (Hoskins and Bretherton 1972, Emanuel 1997).

However, even if one could prolong the period in which the regularized solution could be obtained, in the presence of non-axisymmetric perturbations, one would expect that the annular vortex sheet would be baroclinically unstable on account of the reversal in sign of the radial and vertical gradient of the axisymmetric PV (Montgomery and Shapiro 1995, Schubert et al. 1999, Naylor and Schecter 2014). Questions concerning these and other non-axisymmetric instabilities of the vorticity annulus, as well as longer-term evolution issues, lie beyond the scope of the current study. The reader is referred to Naylor and Schecter (2014), Menelaou et al. (2016), and references cited therein, for further analysis and discussion of these complex topics.

4.1.10 Uniform intensification rate

An interesting feature of the foregoing solution worth remarking on is the approximately uniform intensification rate, at least before regularization of the SE-equation is required[6]. Even beyond that time, there is only a relatively slow increase in spin up as the vortex intensity increases. This finding, which is a feature of all the calculations

---

[6]We remind the reader that we use the term "intensification rate" for the change in the maximum tangential wind speed and not the maximum in the tendency at any point, as the location of these maxima do not, in general, coincide. Thus although the maximum tendency approximately doubles between Fig.3(i) and 3(j), this doubling does not occur at the location of V_{max}.

forced by heating shown below, differs from some previous inferences based on balance theory that the intensification rate should increase as the vortex intensifies because the heating becomes progressively more efficient (Vigh and Schubert 2009 and refs.). An appraisal of ideas relating the efficiency of diabatic heating to the inertial stability is given by Smith and Montgomery (2016b): see also (Kilroy and Smith, 2016, section 7).

We cannot regard the finding of an approximately uniform intensification rate as general, of course, because of the limited number of simulations we have carried out and because the solutions break down at wind speeds approaching minimal hurricane intensity. Most previous theories fix the structure of both the heating rate and the vortex and diagnose the intensification rate at individual times as a function of vortex intensity. In contrast, the present approach is to integrate the balance equations as an initial-value problem so that the vortex structure and, in most experiments the location, but not the structure of the heating, evolve with time. In the experiments with imposed heating, an annulus of cyclonic PV of limited radial extent is generated around the heating region. Thus, prior calculations that assume an increase in vorticity across the entire inner-core would over-estimate the extent of the vorticity increase in comparison. The occurrence of the approximately constant intensification rate found here may be influenced also, in part, by the change in location of the heating relative to the axis of rotation, because the spatial gradients of the heating, and therefore the magnitude of the diabatic forcing term in the SE-equation does not change (see Equation (11) in the appendix).

4.2   Vortex evolution in the Ex-US calculation

Ex-US is similar to Ex-U, but the axis of heating is held fixed, as for example in the calculations by Heng and Wang (2016). The Ex-US simulation is carried out as a benchmark to examine the consequences of allowing the heating axis to move in the Ex-U simulation. Time series of V_{max}, U_{max} and U_{min} for this experiment are included in Fig. 2 and show, perhaps as expected, that intensification rate is impeded in this case. However, there is little difference in the V_{max} curves until after the time when the SE-equation requires regularization, which is merely a minute later in Ex-US. Notwithstanding the previous caveat, a likely reason for the reduced intensification rate is because only those M-surfaces within and beyond the region of heating can be drawn inwards by the heating-induced secondary circulation and the radius to which a given M-surface can be drawn inwards is thereby limited.

The maximum inflow becomes fractionally larger in Ex-US, presumably on account of the slightly weaker vortex, which provides a reduced inertial stability and hence less resistance to radial parcel displacements.

4.3   Vortex evolution in the Ex-S calculation

Figure 7 shows time series of V_{max}, U_{max} and U_{min} for Ex-S, which has a sloping axis of diabatic heating rate. As in Ex-U, V_{max} increases essentially linearly with time, in this case to about 17 h at a rate of approximately 3.9 m s^{-1} (6 h)$^{-1}$, when the rate increases slightly before the integration terminates. At this time, V_{max} has attained a value of 22.4 m s^{-1}. In contrast, U_{min} declines approximately linearly from 1.5 m s^{-1} at the initial time to about 1.2 m s^{-1} at 18 h, while U_{max} has a slight and approximately linear increase from 2.1 m s^{-1} at the initial time to 2.3 m s^{-1} at 13.5 h, followed by a marked increase. Again, at all times, V_{max} and U_{min} are found to occur at the surface while U_{max} occurs in the upper troposphere, between heights of 10 and 13 km. The discriminant of the SE-equation first becomes negative just before 12 h, over 2 h later than in Ex-U.

Figure 8 shows a selection radius-height cross sections for Ex-S. These are similar to those in Figs. 3-4. except that the results are shown only at 16 h, about 4 h after regularization is required, but more than two hours before the solution breaks down. The flow evolution is qualitatively similar to that in Ex-U (compare Figs. 8a-d with the corresponding fields in Figs. 3, but of course, the eyewall updraught slopes outwards with increasing height. As in the Ex-U calculation, U_{min} occurs at the surface, at the base of the low level inflow and V_{max} and its tendency (not shown) occur at the surface where inward advection of the M-surfaces is largest (Fig. 8b). Again, there is strong ascent in the heating region and subsidence elsewhere, both inside and outside the heating region (Fig. 8c). The subsidence is strongest inside the heating region and its strength increases as the heating region contracts (not shown), but the subsidence inside the heating region is marginally stronger over a larger vertical depth than in Ex-U (compare Fig. 8c with the corresponding panels in Fig. 3). Again the M-surfaces are generally not congruent with the streamlines in the upper troposphere.

As in Ex-U, the PV become amplified in an annular region centred on the axis of diabatic heating rate (Fig. 8f), but in Ex-S, narrow sloping regions of low PV develop in the middle to upper troposphere on either side of the axis of maximum heating rate and by 16 h, these have formed into regions with negative PV and, hence, negative Δ (Fig. 8e). Again, the formation of these symmetrically-unstable regions may be understood by examining the structure of the forcing terms α and β in Eq. (10). At 16 h, the α term exhibits an emerging tripole structure, with a small negative tendency appearing on the inside of the positive tendency region (Fig. 8g). The structure of β shows a positive PV tendency at low-levels and a negative PV tendency at upper-levels above the axis of maximum heating (Fig. 8h). This structure resembles a vertical dipole and reflects the positive vertical gradient of heating at low levels and the negative vertical gradient at upper levels above the heating axis. The combined effect of the β and α terms is to produce an outward sloping annulus of elevated (cyclonic) PV in
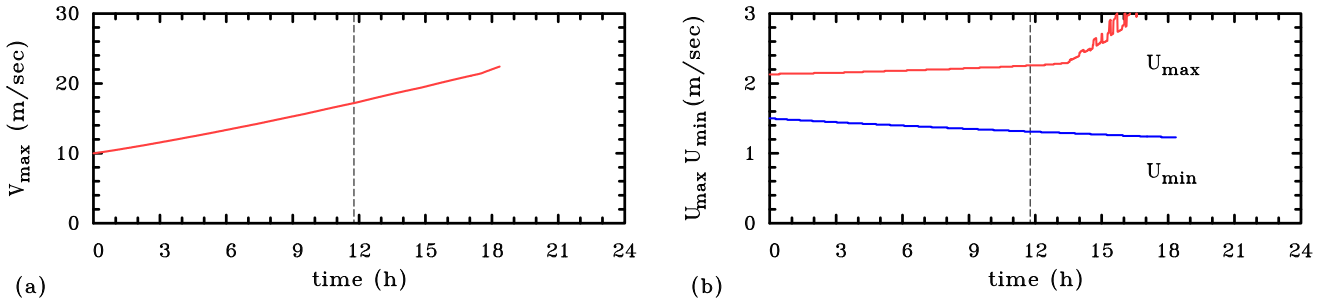
Figure 7. Time series of (a) V_{max}, (b) U_{max}, U_{min} for Ex-S. The dashed vertical line indicates the time at which the regularization is first required.

the main updraught, with reduced values of PV on both sides of the annulus.

Panel (i) of Fig. 8 shows the tangential wind tendency in Ex-S at 16 h, which has a slightly different structure to that in Fig. 6e with the appearance of a tongue of strong spin down tendency on the upper side of the heating axis. However, below this axis, there is a region of strong positive tendency extending to above 11 km as in the calculations with upright heating distributions. Again, this positive tendency may be attributed to the vertical advection of M and it occurs in a region where there is predominantly outflow.

Finally, the complete breakdown of the solution is due to the appearance and growth of small-scale features in the secondary circulation in the upper troposphere, near the edge of where $\Delta < 0$ and the solution is terminated when the potential radius becomes negative at some grid point (not shown).

4.4   Vortex evolution in the Ex-FO calculation

Ex-FO was carried out to investigate the frictional spin down of a balanced vortex in the absence of diabatic heating to force spin up. This problem was examined in the context of a homogeneous vortex by Eliassen and Lystad (1977) and Montgomery et al. (2001). Figure 9a shows time series of V_{max} at the surface and at heights of 1 and 2 km in this simulation as well as the time at which the regularization procedure is first required just before 16 h. It is seen that there is a comparatively rapid spin down of the surface tangential wind component from 10 m s^{-1} at the initial time to less than 6 m s^{-1} at 24 h, whereas the rate of spin down becomes progressively less as the height increases.

Figure 9b shows the radial and tangential wind components in relation to the M-surfaces at the initial time. The imposition of surface friction leads to a shallow layer of inflow near the surface with a weaker and somewhat deeper outward return flow above the inflow. The maximum return flow occurs at an altitude of about 1 km. As is well known, the spin down of the vortex above the surface is a result of the generalized Coriolis force $-(v/r + f)u$ and this is

confined to the height range where the radial outflow is appreciable. The shallowness of the return flow is a reflection of the stable stratification. Above the return flow, the spin down of the tangential circulation is minimal.

At about 16 h, the frictionally-induced overturning circulation leads to a local overturning of the isentropes near the axis of rotation and thereby to static instability at these grid points. This instability is removed by the regularization procedure.

Clearly, spin up of the vortex would require diabatic heating to induce inflow of sufficient strength to negate the frictionally-induced outflow above the inflow layer. In the simple representation of friction considered here, the tangential component of frictional stress is reduced as the surface flow weakens and so, therefore, does the secondary circulation induced by the friction (blue dashed curve in Fig. 10). We investigate the combined effects of friction and diabatic heating in the next subsection.

4.5   Vortex evolution in the Ex-UF calculation

We examine now the effects of surface friction on the balanced vortex evolution in the presence of diabatic heating as formulated in the Ex-U calculation. Figure 10 shows time series of V_{max}, U_{max} and U_{min} for Ex-UF and Ex-FO and compares the time series for V_{max} and U_{min} with those for Ex-U[7]. In the Ex-UF calculation, V_{max} increases approximately linearly from 10 m s^{-1} at $t = 0$ h to about 17.1 m s^{-1} at $t = 24$ h, a bit over an hour before the solution breaks down. The solution requires regularization to be applied at 9 h, just before the time it is required in Ex-U, but it breaks down a bit over an hour earlier than in Ex-U. Notably, in the presence of near-surface friction U_{min} is roughly twice as large compared with its values in the no friction calculations: at $t = 0$ h its magnitude is about 3.2 m s^{-1} compared with 1.5 m s^{-1} in the case without friction. Neither U_{min} nor U_{max} change appreciably during the simulation, both showing only a tiny increase. In

---

[7]The curve U_{max} for Ex-U is virtually coincident with that for Ex-UF and for this reason is not shown.
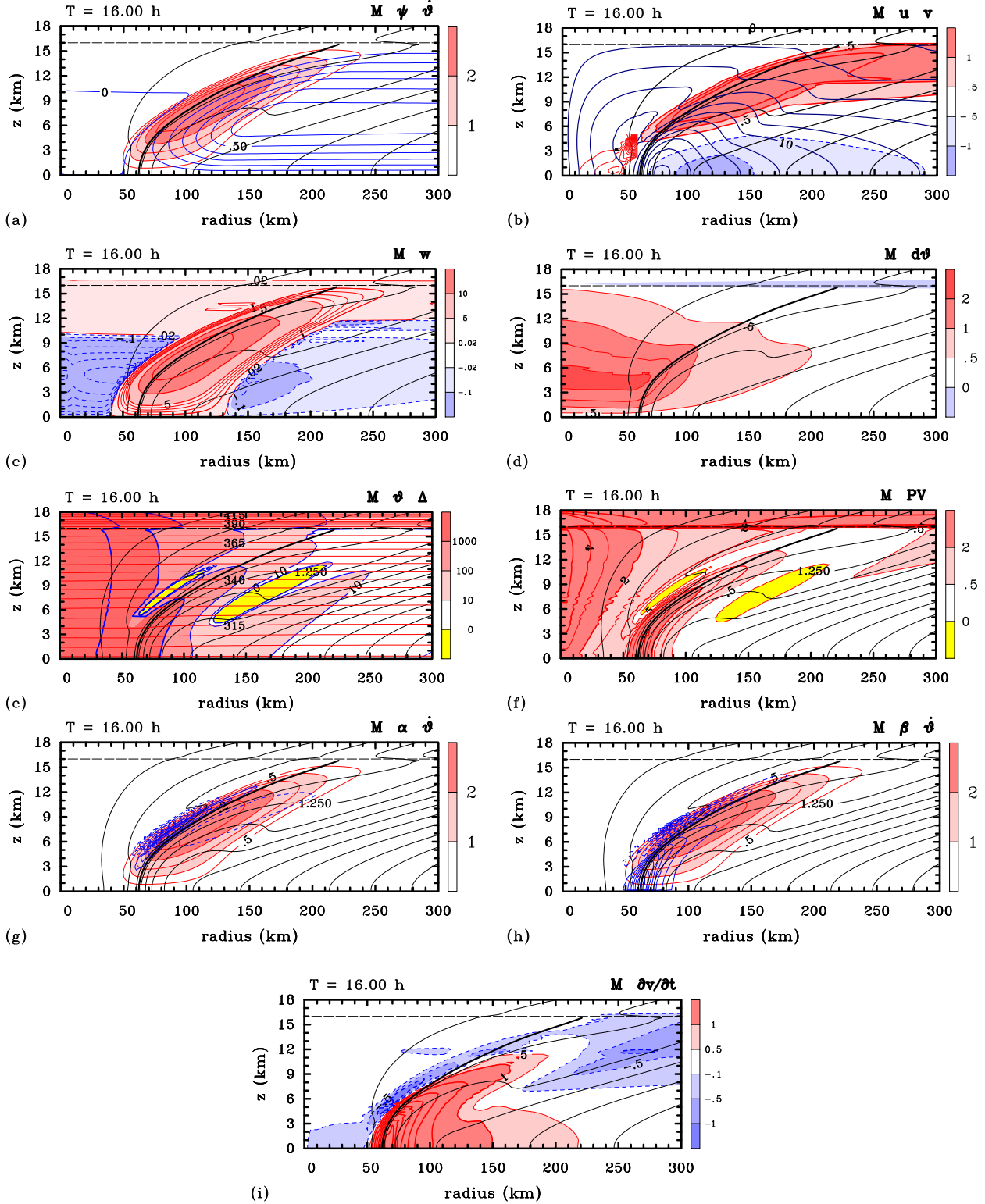
Figure 8. Representative fields for Ex-S at 16 h. Legend otherwise as for panels (a)-(d) in Fig. 3; panels (a), (c), (e) and (g) in Fig. 4, and panel (e) in Fig. 3 about 4 h after regularization is required. Thin solid (red) contours below 5 km height and inside 60 km radius in panel (b) are those of radial outflow with contour interval 0.02 m s^{-1}.

contrast to its behaviour in Ex-U and Ex-S, U_{max} remains relatively smooth until the end of the simulation.

Figure 11 shows a selection of radius-height cross sections for Ex-UF, similar to those in Figs. 3c, 4c, 3a and 3j
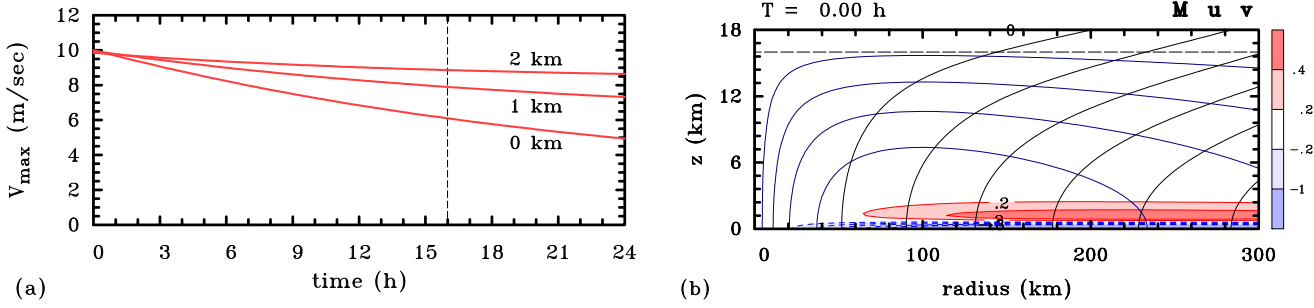
Figure 9. Results for Ex-FO. (a) Time series of maximum tangential wind component (here V_{max}) at the surface and at heights of 1 and 2 km. (b) Radius-height cross sections of M-surfaces superimposed on the radial and tangential wind components, u and v, respectively. Contour intervals: for M, 5×10^5 m^2 s^{-1}; for u (shaded), 0.2 m s^{-1} down to -1 m s^{-1}, 1 m s^{-1} for lower values (negative contours dashed); for v, 2 m s^{-1}. The thin dashed vertical line indicates the time at which the solution requires regularization.
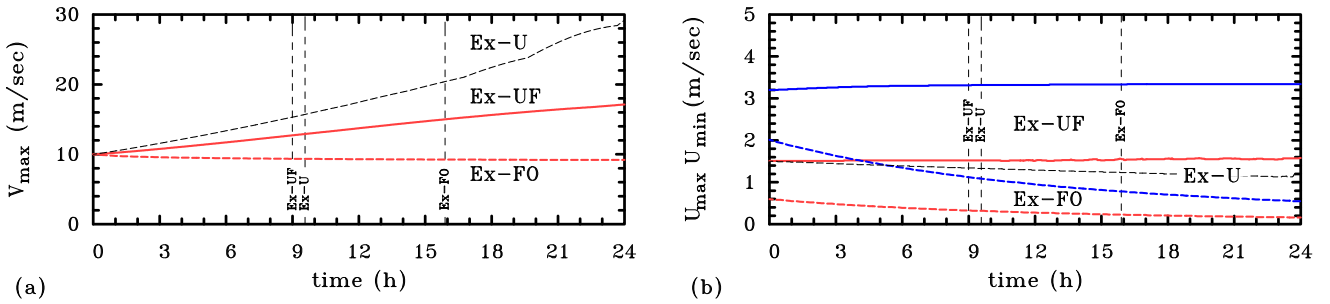
.

Figure 10. Comparison of time series of (a) V_{max} and (b) U_{max} (red), U_{min} (blue) in Ex-UF (solid curves), Ex-U (thin dashed black curves) and Ex-FO (dashed curves). The thick black solid curve marks the M-surface along which the heating axis is aligned. To avoid clutter, we have not plotted U_{max} for Ex-U: this is shown in Fig. 2.

at selected times. Perhaps of most significance in comparing the radial motion between Ex-UF and Ex-U is the fact that the near-surface inflow is much stronger at most radii. The stronger inflow is a result of the additional frictionally-induced inflow not present in Ex-U[8]. The shallow surface-based outflow seen at small radii in Figs. 3c, d and 4b no longer occurs: with friction, there is now weak inflow in this region (Figs. 11a and b), but there remains an elevated region of low-level outflow induced by the heating.

Unlike the case of Ex-U, where V_{max} occurs at the surface, in Ex-UF, V_{max} occurs above about 2 km, still within a region of significant radial inflow ($U_{min} > 1$ m s^{-1}), but above the layer of strongest inflow.

Figures 11c and 11d show the PV fields at 9 h and 16 h for Ex-UF. These should be compared with those for Ex-U shown in Figs. 4d and 6h, respectively. It is seen that the

differences are confined primarily to the lower troposphere (below about 5 km) and that the regions of negative PV are practically the same. Presumably, it is for this reason, the breakdown of the two solutions is similar and occurs in the upper troposphere. The shallow tongues of positive PV at low levels near the axis are associated primarily with a shallow layer of enhanced static stability near the surface. This layer results from a cold anomaly, θ' in the friction layer, which is a consequence of the balance assumption in combination with the friction layer being one in which $\partial v/\partial z > 0$.

It may be worth noting that from 13.6 h onwards, a region of negative static stability develops on account of the frictionally-induced overturning circulation, but the effects of this instability in solving the SE-equation are removed by the regularization procedure.

Figures 11e and 11f show, inter alia, the streamfunction and tangential wind tendency fields at 16 h, similar to Figs. 6a and 6e. As in the case without friction (Fig. 6), much of the low level inflow passes through the heated region and there is a positive tangential wind tendency through much of the heated region. Again, in the upper

---

[8]Note that in the present calculations, the linearity of the SE-equation implies that the frictional effects of the boundary layer in producing inflow are additive to those of the convective heating. However, this will not be true in general because the boundary layer in the inner core region of a tropical cyclone is intrinsically nonlinear except, perhaps, at very low maximum tangential wind speeds of a few m s^{-1} (see e.g. Smith and Montgomery 2015, Sec. 5; Abarca et al. 2016).
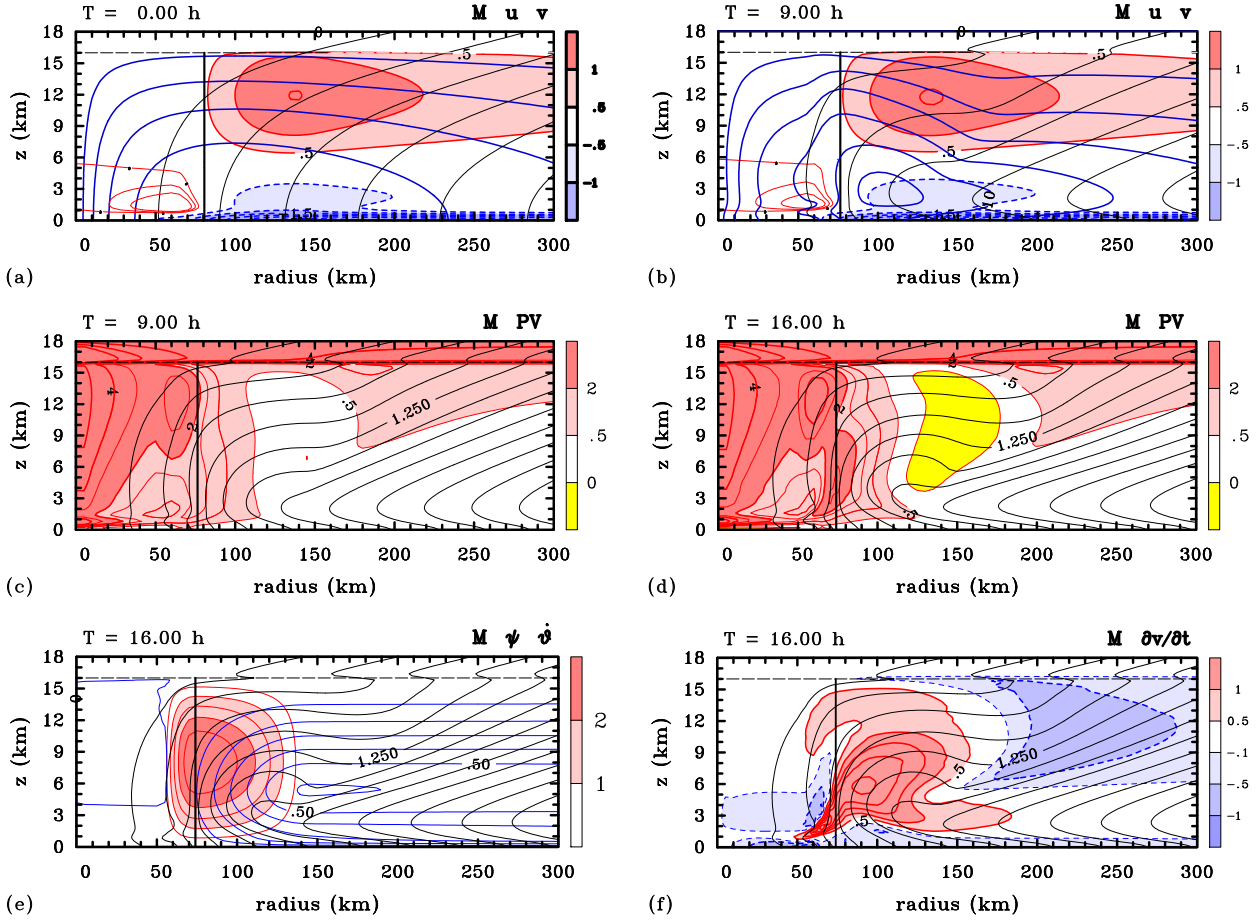
Figure 11. Results for Ex-UF. (a) and (b) as for panel (c) and (d) in Fig. 3, except that the thin contours showing outflow in the lower troposphere, inside the heating region, have a spacing of 0.02 m s^{-1} starting with the zero contour. (c) and (d) as for panel (c) in Fig. 5, but at 9 h and 16 h, respectively. Panels (e) and (f) show, inter alia, the streamfunction and tangential wind tendency fields at 16 h, similar to Figs. 6a and 6e, respectively.

troposphere, the positive tendency occurs in a region of radial outflow. However in the lower troposphere the positive tendency is a result of both the radial and vertical advection of M. Notably, in contrast to Ex-U, there is a negative tangential wind tendency at low levels on account of friction (compare Fig. 11f with 6e) and the lofting of frictionally reduced M into the heated region. The negative tangential wind tendency at low levels is perhaps not realistic for an intensifying vortex and is possibly a limitation of assuming balance in the boundary layer, effectively suppressing the nonlinear boundary layer spin up mechanism (Smith and Montgomery 2016a). Another possibility is that the frictional spin down tendency is too strong for the prescribed heating. In future work we plan to examine the relationship between the strength of convective forcing in relation to that of friction in more detail.

It is interesting to compare the solution structure in the Ex-UF calculation with the one calculation including heating and friction shown in Fig. 13 of Pendergrass and Willoughby (2009). In their figure, the flow above the frictional boundary layer beyond the heating region is mostly outwards, the exception being a local region of weak inflow inside a radius of 50 km. This pattern of secondary circulation would imply that the vortex would be spinning down in such regions unless the vertical advection of angular momentum were able to compensate locally (this situation would appear not to be the case in Fig. 13 of Pendergrass and Willoughby because the radial outflow spans a region over which the vertical velocity is very small). In their calculation, it would appear that the boundary layer induced outflow in the lower troposphere dominates the heating-induced inflow. Equivalently the heating-induced ascent in the eyewall is too weak to ventilate the mass converging in the boundary layer. This behaviour is different from that in the Ex-UF calculation shown in Fig. 11, where the flow in the lower troposphere outside the heating region is radially inwards over a layer approximately 5 km deep out to a radius of 300 km. The implied spin down in the Pendergrass and Willoughby calculation would be more transparent in a prognostic framework.

The foregoing comparison points to limitations of performing diagnostic calculations by themselves as opposed to an integration of an initial value problem. For example, Pendergrass and Willoughby's vortices have maximum tangential velocities of 50 m s^{-1}, whereas in all the present prognostic balance calculations starting with a tangential wind maximum of 10 m s^{-1}, breakdown of the solutions occurs at maximum wind speeds close to 30 m s^{-1}. Notwithstanding the fact that the prognostic system may have its own limitations, this finding raises the possibility that not all strong vortices used as starting points for diagnostic calculations may be attainable from pathways involving balanced evolution from an initial vortex of only modest intensity. Clearly, further work is required to explore this possibility.

5 Discussion and conclusions

The axisymmetric balance model calculations presented herein provide a benchmark for understanding the classical spin up mechanism for tropical cyclone intensification, which refers to the convectively-induced inward radial advection of absolute angular momentum (M) at levels where this quantity is materially conserved. The role of this mechanism in the spin up of the eyewall (the heating region) was investigated for a range of heating configurations, both in an inviscid model and one with a balanced frictional boundary layer. It was shown that, beyond the heating region, the flow is quasi-horizontal and spins up by the classical mechanism. Much of the heating-induced inflow ascends in the heating region and flows outwards in the upper troposphere. In the lower half of the heating region, the secondary circulation has a local component of flow *both inwards and upwards* across the M-surfaces towards low values of M, i.e. the vertical advection of M becomes important in spinning uresults from previous studiesresults from previous studiesp the eyewall. In the upper part of the eyewall, positive tangential wind tendencies are found in regions of radial outflow and in these regions, the vertical advection of M is the dominant spin up process.

In the cases without friction, there is weak outflow at low levels inside the annulus of heating as well as inflow beyond this annulus. This deformation flow pattern, in the presence of a radial gradient of M, leads to a spatial concentration of M-surfaces near this axis. The effect is akin to a frontogenesis process with M serving as the frontogenetic element. This process tends toward a discontinuity in M and amplifies the vorticity towards a vortex sheet. Whether this vortex sheet materializes in a finite time remains an open question in general, but can be expected to depend on the chosen parameters in the model.

In all the flows with heating, the vortex intensification rate hardly changes, at least before appreciable regions of symmetric instability have developed. This finding does not support the idea that spin-up increases markedly as the vortex intensity increases, a finding that is in contrast to some previous results. However, as discussed in the text,

there are some differences in the formulation of the present model and previous ones and the integrations only reach minimal hurricane intensity before they break down so that general conclusions from this finding cannot be drawn.

The axisymmetric balance solutions can be integrated only for a finite time before the discriminant (and potential vorticity) of the SE-equation becomes negative and a regularization procedure becomes necessary to keep the equation globally elliptic. Beyond this time, the solutions eventually become noisy in the upper troposphere as the regions with negative discriminant before regularization become larger in size. The integrity of the solutions after the discriminant (and potential vorticity) becomes appreciably negative is unclear, in part because of the expectation that symmetric instability will occur at small-scale (e.g. Thorpe and Rotunno 1989) and also because of hydrodynamic shear instability and mesovortices that are expected to develop on the emerging vortex sheet on the inside of the eyewall (Montgomery et al. 2002, Naylor and Schecter 2014, and refs.). Furthermore, it does not appear that the streamlines and M-surfaces are becoming congruent in the upper troposphere on the time-scale over which the solutions break down, calling into question the existence of a quasi-steady state, even in the inner-core region. This finding would appear to have implications for assumed steady state models such as that of Emanuel (1986) and later incarnations thereof (e.g. Emanuel 2012).

The work described herein was motivated in part by the desire to understand how the tropical cyclone eyewall spins up in numerical model simulations and in the real atmosphere if the air within the eyewall has a radially-outward component after leaving the boundary layer. A related question is whether the classical paradigm for tropical cyclone intensification can be utilized in such an explanation. Exemplified by the range of calculations carried out, it would appear that the classical paradigm for intensification cannot explain the spin up of the eyewall in the lower troposphere if the air within the eyewall is moving radially outwards. In all the calculations shown, spin up of the lower portion of the eyewall occurs by the classical mechanism in conjunction with the vertical advection of M. In the calculation with boundary layer friction, spin down occurs in the friction layer. Nevertheless, in the upper part of the heating region, there are regions where the vertical advection of M is sufficiently large that a positive spin up tendency occurs even in regions of radial outflow.

In a strictly axisymmetric balanced model (see footnote 2), or in a generalized balanced flow consisting of gradient wind balance above the boundary layer and Ekman-like balance in the boundary layer (e.g. Abarca et al. 2015), the vertical gradient of M in the boundary layer is positive. Clearly, for sustained spin up to occur anywhere where there is radial outflow, there are two possibilities. Either there must be a sufficiently-large negative vertical gradient of M above the boundary layer to permit the vertical advection of M to dominate the spin down tendency accompanying radial advection, or there must be a source of high M

in the boundary layer. There may, of course be a temporary spin up depending on the structure of the initial vortex, but without a low-level source of M, by for example the classical mechanism or from the boundary layer, the spin up cannot be maintained.

It has been shown in recent work that, in an axisymmetric configuration, the spin up of supergradient tangential winds in the boundary layer can provide the necessary negative vertical gradient of M to spin up the eyewall (Schmidt and Smith 2016, Persing et al. 2013, Fig. 12(d)). However, in a three-dimensional configuration, there is evidence that the spin up of the eyewall in the lower troposphere is accomplished by resolved eddy momentum fluxes (Persing et al. 2013, cf .Fig. 10(d), (g) and (h); Kilroy 2018, personal communication).

6 Appendix

The SE-equation, Eq. (3) may be written in the form:

$$\frac{\partial}{\partial r}\left[\bar{A}\frac{\partial \psi}{\partial r} + \frac{1}{2}\bar{B}\frac{\partial \psi}{\partial z}\right] + \frac{\partial}{\partial z}\left[\bar{C}\frac{\partial \psi}{\partial z} + \frac{1}{2}\bar{B}\frac{\partial \psi}{\partial r}\right] = \dot{\Theta},$$
(11)

where

$$\bar{A} = -g\frac{\partial \chi}{\partial z}\frac{1}{\rho r} = \left(\frac{\chi}{\rho r}\right)N^2,$$

$$\bar{B} = -\frac{2}{\rho r}\frac{\partial}{\partial z}(\chi C) = -\frac{2}{\rho r}\left(\chi \xi \frac{\partial v}{\partial z} + C\frac{\partial \chi}{\partial z}\right),$$

$$\bar{C} = \left(\xi(\zeta + f)\chi + C\frac{\partial \chi}{\partial r}\right)\frac{1}{\rho r} = \chi I_g^2,$$

and

$$\dot{\Theta} = g\frac{\partial}{\partial r}\left(\chi^2\dot{\theta}\right) + \frac{\partial}{\partial z}\left(C\chi^2\dot{\theta}\right) + g\frac{\partial F_\lambda}{\partial r} + \frac{\partial}{\partial z}\left(\chi\xi F_\lambda\right),$$

where N is the Brunt-Väisälä frequency defined as $(g/\theta)\partial\theta/\partial z$ and I is the generalized inertial frequency defined by $I^2 = \xi(\zeta + f) + \frac{C}{\chi}\frac{\partial \chi}{\partial r}$. It follows that $\bar{A}$ and $\bar{C}$ characterize the static stability and inertial stability, respectively. Further, B characterizes, in part, the strength of the vertical shear.

Equation (11) may be written alternatively as:

$$\bar{A}\frac{\partial^2 \psi}{\partial r^2} + \bar{B}\frac{\partial^2 \psi}{\partial z \partial r} + \bar{C}\frac{\partial^2 \psi}{\partial z^2} + \bar{E}\frac{\partial \psi}{\partial r} + \bar{F}\frac{\partial \psi}{\partial z} = \dot{\Theta}, \quad (12)$$

where

$$\bar{E} = \frac{\partial \bar{A}}{\partial r} + \frac{1}{2}\frac{\partial \bar{B}}{\partial z},$$

and

$$\bar{F} = \frac{\partial \bar{C}}{\partial z} + \frac{1}{2}\frac{\partial \bar{B}}{\partial r}.$$

Equation (12) is an elliptic equation provided that the discriminant, $\Delta = 4\bar{A}\bar{C} - \bar{B}^2 > 0$. For a vortex that is both statically stable and inertially stable, N^2 and I^2 are both positive and provided that the vertical shear is not too large, the criterion for ellipticity is everywhere satisfied. Typically,

this is the case for the initial vortices studied here. However, as the vortex evolves, small regions develop in which the flow is inertially unstable $I^2 < 0$, or in which the shear is sufficiently large locally to make $\Delta < 0$. In this case, the vortex is symmetrically unstable and to advance the solution for v further in time, it is necessary to regularize the equation for ψ by removing the regions of symmetric instability ($\Delta < 0$).

To accomplish the regularization we follow the procedure adopted by Möller and Shapiro (2002). First, having calculated new coefficients $\bar{A}$, $\bar{B}$ and $\bar{C}$ at a particular time, we search for points at which $\Delta < 0$ and, assuming first that $\bar{A}$ we calculate the minimum value of $\bar{C}$ at these points, say $\bar{C}_{min}$. Then, at points where $\Delta < 0$ we increase $\bar{C}$ by adding $1.01\bar{C}_{min}$. If $\bar{A} < 0$ at any of these points, i.e. if the flow is statically unstable there, we set N^2 in the expression for $\bar{A}$ to 1×10^{-8} s^{-2}. The next step is to recalculate $\Delta < 0$ using the new values of $\bar{C}$ and possibly $\bar{A}$. Now, at any remaining points where $\Delta < 0$, the vertical shear and therefore $\bar{B}$ must be too large since $\bar{C}$ and $\bar{A}$ are both positive. At these points we effectively reduce the shear by setting $\Delta = 2\bar{A}\bar{C}$ and replacing $\bar{B}$ by $\sqrt{2\bar{A}\bar{C}}$.

References

Abarca, S. F. and M. T. Montgomery, 2014: Departures from axisymmetric balance dynamics during secondary eyewall formation. *J. Atmos. Sci.*, **71**, 3723–3738.

Abarca, S. F., M. T. Montgomery, S. A. Braun, and J. Dunion, 2016: On secondary eyewall formation of Hurricane Edouard (2014). *Mon. Wea. Rev.*, **144**, 3321–3331.

Abarca, S. F., M. T. Montgomery, and J. C. McWilliams, 2015: The azimuthally averaged boundary layer structure of a numerically simulated major hurricane. *J. Adv. Model. Earth Syst.*, **7**, 1207–1219.

Bui, H. H., R. K. Smith, M. T. Montgomery, and J. Peng, 2009: Balanced and unbalanced aspects of tropical-cyclone intensification. *Quart. Journ. Roy. Meteor. Soc.*, **135**, 1715–1731.

Dunion, J. P., 2011: Rewriting the climatology of the tropical north atlantic and caribbean sea atmosphere. *J. Clim.*, **24**, 893–908.

Eliassen, A., 1962: On the vertical circulations in frontal zones. *Geofys. Publ.*, **24**, 147–160.

Eliassen, A. and M. Lystad, 1977: The Ekman layer of a circular vortex: A numerical and theoretical study. *Geophys. Norv.*, **31**, 1–16.

Emanuel, K. A., 1986: An air-sea interaction theory for tropical cyclones. Part I: Steady state maintenance. *J. Atmos. Sci.*, **43**, 585–604.

— 1995: The behavior of a simple hurricane model using a convective scheme based on subcloud-layer entropy equilibrium. *J. Atmos. Sci.*, **52**, 3960–3968.

— 1997: Some aspects of hurricane inner-core dynamics and energetics. *J. Atmos. Sci.*, **54**, 1014–1026.

— 2012: Self-stratification of tropical cyclone outflow. Part II: Implications for storm intensification. *J. Atmos. Sci.*, **69**, 988–996.

Fang, J. and F. Zhang, 2011: Evolution of multiscale vortices in the development of Hurricane Dolly (2008). *J. Atmos. Sci.*, **68**, 103–122.

Hack, J. J. and W. H. Schubert, 1986: Nonlinear response of atmospheric vortices to heating by organized cumulus convection. *J. Atmos. Sci.*, **43**, 1559–1573.

Heng, J. and Y. Wang, 2016: Nonlinear response of a tropical cyclone vortex to prescribed eyewall heating with and without surface friction in tcm4: Implications for tropical cyclone intensification. *J. Atmos. Sci.*, **73**, 1315–1333.

Hoskins, B. J. and F. P. Bretherton, 1972: Atmospheric frontogenesis models: Mathematical formulation snd solution. *J. Atmos. Sci.*, **29**, 11–37.

Kilroy, G. and R. K. Smith, 2016: A numerical study of deep convection in tropical cyclones. *Quart. Journ. Roy. Meteor. Soc.*, **142**, 3138–3151.

McIntyre, M. E., 2008: Fundamentals of atmosphere-ocean dynamics. *LATEX version edited by Bj́orn Habler and Christophe Koudella, with assistance from Teresa Cronin and Sarah Shea-Simonds*, 244.

McWilliams, J. C., 2011: *Fundamentals of geophysical fluid dynamics*. Cambridge University Press, Cambridge, England, ISBN-13:978-1107404083, 272pp.

McWilliams, J. C., L. P. Graves, and M. T. Montgomery, 2003: A formal theory for vortex Rossby waves and vortex evolution. *Geophys. Astrophys. Fluid Dyn.*, **97**, 275–309.

Menelaou, K., D. A. Schecter, and M. K. Yau, 2016: On the relative contribution of inertia-gravity wave radiation to asymmetric instabilities in tropical-cyclone-like vortices. *J. Atmos. Sci.*, **73**, 3345–337.

Möller, J. D. and M. T. Montgomery, 2000: Tropical cyclone evolution via potential vorticity anomalies in a three-dimensional balance model. *J. Atmos. Sci.*, **57**, 3366–3387.

Möller, J. D. and R. K. Smith, 1994: The development of potential vorticity in a hurricane-like vortex. *Quart. Journ. Roy. Meteor. Soc.*, **120**, 1255–1265.

Montgomery, M. T., M. E. Nichols, T. A. Cram, and A. B. Saunders, 2006: A vortical hot tower route to tropical cyclogenesis. *J. Atmos. Sci.*, **63**, 355–386.

Montgomery, M. T. and L. J. Shapiro, 1995: Generalized charney-stern and fjortoft theorems for rapidly rotating vortices. *J. Atmos. Sci.*, **52**, 1829–1833.

Montgomery, M. T. and R. K. Smith, 2014: Paradigms for tropical cyclone intensification. *Aust. Met. Ocean. Soc. Journl.*, **64**, 37–66, [Available online at http://www.bom.gov.au/amoj/docs/2014/montgomer

— 2017: Recent developments in the fluid dynamics of tropical cyclones. *Annu. Rev. Fluid Mech.*, **49**, 541–574.

Montgomery, M. T., H. D. Snell, and Z. Yang, 2001: Axisymmetric spindown dynamics of hurricane-like vortices. *J. Atmos. Sci.*, **58**, 421–435.

Montgomery, M. T., V. A. Vladimirov, and P. V. Denissenko, 2002: Recent developments in the fluid dynamics of tropical cyclones. *J. Fluid Mech.*, **471**, 1–32.

Naylor, J. and D. A. Schecter, 2014: Evaluation of the impact of moist convection on the development of asymmetric inner core instabilities in simulated tropical cyclones. *J. Adv. Model. Earth Syst.*, **6**, 1027–1048.

Ooyama, K. V., 1969: Numerical simulation of the life cycle of tropical cyclones. *J. Atmos. Sci.*, **26**, 3–40.

— 1982: Conceptual evolution of the theory and modeling of the tropical cyclone. *J. Meteor. Soc. Japan*, **60**, 369–380.

Paull, G., K. Menelaou, and M. K. Yau, 2017: Sensitivity of tropical cyclone intensification to axisymmetric heat sources: The role of inertial stability. *J. Atmos. Sci.*, **74**, 2325–2340.

Pendergrass, A. G. and H. E. Willoughby, 2009: Diabatically induced secondary flows in tropical cyclones. part i. quasi-steady forcing. *Mon. Wea. Rev.*, **137**, 3–40.

Persing, J., M. T. Montgomery, J. McWilliams, and R. K. Smith, 2013: Asymmetric and axisymmetric dynamics of tropical cyclones. *Atmos. Chem. Phys.*, **13**, 12299–12341.

Rotunno, R., 2014: Secondary circulations in rotating-flow boundary layers. *Aust. Met. Ocean. Soc. Journl.*, **64**, 27–35, [Available online at http://www.bom.gov.au/amoj/docs/2014/rotunno_h

Rozoff, C. M., W. H. Schubert, and J. P. Kossin, 2008: Some dynamical aspects of tropical cyclone concentric eyewalls. *Quart. Journ. Roy. Meteor. Soc.*, **135**, 583–593.

Schmidt, C. J. and R. K. Smith, 2016: Tropical cyclone evolution in a minimal axisymmetric model revisited. *Quart. Journ. Roy. Meteor. Soc.*, **142**, 1505–1516.

Schubert, W. H. and B. T. Alworth, 1982: Evolution of potential vorticity in tropical cyclones. *Quart. Journ. Roy. Meteor. Soc.*, **39**, 1687–1697.

Schubert, W. H. and J. J. Hack, 1982: Inertial stability and tropical cyclone development. *J. Atmos. Sci.*, **39**, 1687–1697.

Schubert, W. H., M. T. Montgomery, R. K. Taft, T. A. Guinn, S. R. Fulton, J. P. Kossin, J. P. Edwards, C. M. Rozoff, J. L. Vigh, B. D. McNoldy, and J. P. Kossin, 1999: Polygonal eyewalls, asymmetric eye contraction, and potential vorticity mixing in hurricanes. *J. Atmos. Sci.*, **56**, 1197–1923.

Schubert, W. H., C. J. Slocum, and R. K. Taft, 2016: Forced, balanced model of tropical cyclone intensification. *J. Met. Soc. Japan*, **94**, 119–135.

Schubert, W. H., C. J. Slocum, J. L. Vigh, B. D. McNoldy, and J. P. Kossin, 2007: On the distribution of subsidence in the hurricane eye. *Quart. Journ. Roy. Meteor. Soc.*, **133**, 1–20.

Shapiro, L. J. and M. T. Montgomery, 1993: A three-dimensional balance theory for rapidly-rotating vortices. *J. Atmos. Sci.*, **50**, 3322–3335.

Shapiro, L. J. and H. Willoughby, 1982: The response of balanced hurricanes to local sources of heat and momentum. *J. Atmos. Sci.*, **39**, 378–394.

Smith, R. K., 1981: The cyclostrophic adjustment of vortices with application to tropical cyclone modification. *J. Atmos. Sci.*, **38**, 2020–2030.

— 2006: Accurate determination of a balanced axisymmetric vortex. *Tellus A*, **58**, 98–103.

Smith, R. K., G. Kilroy, and M. T. Montgomery, 2014: Why do model tropical cyclones intensify more rapidly at low latitudes? *J. Atmos. Sci.*, **140**, 1783–1804.

Smith, R. K. and M. T. Montgomery, 2008: Balanced depth-averaged boundary layers used in hurricane models. *Quart. Journ. Roy. Meteor. Soc.*, **134**, 1385–1395.

— 2015: Towards clarity on understanding tropical cyclone intensification. *J. Atmos. Sci.*, **72**, 3020–3031.

— 2016a: Comments on: Nonlinear response of a tropical cyclone vortex to prescribed eyewall heating with and without surface friction in tcm4: Implications for tropical cyclone intensification, by J. Heng and Y. Wang. *J. Atmos. Sci.*, **73**, 5101–5103.

— 2016b: The efficiency of diabatic heating and tropical cyclone intensification. *Quart. Journ. Roy. Meteor. Soc.*, **142**, 2081–2086.

Smith, R. K., M. T. Montgomery, and S. V. Nguyen, 2009: Tropical cyclone spin up revisited. *Quart. Journ. Roy. Meteor. Soc.*, **135**, 1321–1335.

Smith, R. K., M. T. Montgomery, and H. Zhu, 2005: Buoyancy in tropical cyclone and other rapidly rotating atmospheric vortices. *Dyn. Atmos. Oceans*, **40**, 189–208.

Stern, D. P., J. L. Vigh, D. S. Nolan, and F. Zhang, 2015: Revisiting the relationship between eyewall contraction and intensification. *J. Atmos. Sci.*, **72**, 1283–1306.

Sundqvist, H., 1970a: Numerical simulation of the development of tropical cyclones with a ten-level model. Part I. *Tellus*, **4**, 359–390.

— 1970b: Numerical simulation of the development of tropical cyclones with a ten-level model. Part II. *Tellus*, **5**, 505–510.

Thorpe, A. J. and R. Rotunno, 1989: Nonlinear aspects of symmetric instability. *J. Atmos. Sci.*, **46**, 1285–1299.

Vigh, J. L. and W. H. Schubert, 2009: Rapid development of the tropical cyclone warm core. *J. Atmos. Sci.*, **66**, 3335–3350.

Wang, Y. and H. Wang, 2013: The inner-core size increase of Typhoon Megi (2010) during its rapid intensification phase. *Trop. Cyclone Res. Rev.*, **2**, 65–80.

Willoughby, H. E., 1979: Forced secondary circulations in hurricanes. *J. Geophys. Res.*, **84**, 3173–3183.

Wirth, V. and T. J. Dunkerton, 2006: A unified perspective on the dynamics of axisymmetric hurricanes and monsoons. *J. Atmos. Sci.*, **63**, 2529–2547.

Xu, J. and Y. Wang, 2010: Sensitivity of tropical cyclone inner-core size and intensity to the radial distribution of surface entropy flux. *J. Atmos. Sci.*, **67**, 1831–1852.

Zhang, J. A. and F. D. Marks, 2015: Effects of horizontal diffusion on tropical cyclone intensity change and structure in idealized three-dimensional numerical simulations. *Mon. Wea. Rev.*, **48**, 3981–3995.